JGR Atmospheres

RESEARCH ARTICLE
10.1029/2025JD044471

Key Points:

- Analysis of the moist static energy budget reveals key processes driving monsoon burst evolution
- Climate models exhibit variability in burst evolution, with MRI-ESM2-0 showing realistic transitions and BCC-CSM2-MR showing abrupt change
- Thermodynamic moisture advection and dynamic wind patterns influence precipitation changes differently across models

Correspondence to:
M. S. Singh,
martin.singh@monash.edu

Citation:
Mohanty, S., Jakob, C., & Singh, M. S. (2026). The moist static energy budget of Australian summer monsoon bursts in climate models: Insights from present and warming climate scenarios. *Journal of Geophysical Research: Atmospheres*, *131*, e2025JD044471. https://doi.org/10.1029/2025JD044471

Received 29 MAY 2025
Accepted 25 JAN 2026

Author Contributions:
Conceptualization: Sarthak Mohanty, Christian Jakob, Martin S. Singh
Data curation: Sarthak Mohanty
Formal analysis: Sarthak Mohanty, Christian Jakob, Martin S. Singh
Funding acquisition: Christian Jakob, Martin S. Singh
Investigation: Sarthak Mohanty, Christian Jakob, Martin S. Singh
Methodology: Sarthak Mohanty, Christian Jakob, Martin S. Singh
Project administration: Christian Jakob, Martin S. Singh
Resources: Sarthak Mohanty
Software: Sarthak Mohanty
Supervision: Christian Jakob, Martin S. Singh
Validation: Sarthak Mohanty
Visualization: Sarthak Mohanty, Christian Jakob, Martin S. Singh

The Moist Static Energy Budget of Australian Summer Monsoon Bursts in Climate Models: Insights From Present and Warming Climate Scenarios

Sarthak Mohanty[1,2,3], **Christian Jakob**[1,4], **and Martin S. Singh**[1,4]

[1]School of Earth, Atmosphere and Environment, Monash University, Melbourne, VIC, Australia, [2]Center for Climate Physics, Institute for Basic Science, Busan, Republic of Korea, [3]Pusan National University, Busan, Republic of Korea, [4]ARC Centre of Excellence for the Weather of the 21st Century, Melbourne, VIC, Australia

Abstract This study investigates the complex dynamics of burst evolution in the Australian summer monsoon under present-day and warmer climate conditions. Using reanalysis data, historical atmosphere-only simulations (AMIP), and simulations with uniformly increased sea surface temperatures (+4K; AMIP+4K), we examine how seasonal-mean precipitation and burst behavior respond to warming across eight climate models. A consistent link emerges between higher seasonal-mean precipitation and a greater number of bursts. A moist static energy budget analysis reveals that horizontal moisture advection governs burst evolution, while model-specific parameterizations add variability in burst characteristics. Some models show gradual transitions governed by horizontal moisture advection, others display abrupt shifts absent in reanalysis. Among the three models with AMIP+4K simulations, MRI-ESM2-0 and BCC-CSM2-MR reproduce seasonal precipitation patterns close to their AMIP counterparts, with burst frequencies nearly unchanged in BCC-CSM2-MR and slightly reduced in MRI-ESM2-0. Only MRI-ESM2-0 captures a gradual, physically consistent burst evolution resembling reanalysis, whereas BCC-CSM2-MR still shows abrupt transitions. IPSL-CM6A-LR, the third model with AMIP+4K simulations, shows a gradual evolution but produces stronger mean precipitation and fewer bursts—contrary to the typical positive precipitation–burst relationship. Cluster-based composites show that precipitation changes arise from differing contributions of thermodynamic and dynamic components of vertical moisture advection. In MRI-ESM2-0, enhanced precipitation in warming scenarios is mainly driven by stronger thermodynamic moistening, whereas in IPSL-CM6A-LR, dynamically induced drying offsets thermodynamic gains, particularly in specific burst clusters. These results emphasize model-dependent monsoon burst responses and the need to separate dynamic and thermodynamic influences to strengthen confidence in future hydro-climate projections.

Plain Language Summary The Australian Summer Monsoon (ASM) brings crucial rainfall to northern Australia between October and April, supporting agriculture and ecosystems. Although we have learned more about the ASM, climate models still show big differences in how they predict short-term rainfall events, or "monsoon bursts," and how these might change with global warming. In this study, we explore how different climate models simulate these bursts and what is the mechanism behind it. We compare current climate data to future warming scenarios, with a focus on moisture and energy transport as they influence burst behavior. We discovered that in some models, more rain falls because there is more moisture in the air, whereas in others, shifting wind patterns reduce rainfall. These differences demonstrate how models behave differently, with moisture and wind both playing important roles. Understanding these model differences allows us to improve our predictions of how rainfall patterns will change, which helps us prepare for future risks such as floods or droughts in northern Australia.

1. Introduction

The Australian Summer Monsoon (ASM) represents a seasonal reversal of the circulation between winter and summer over Australia's tropical north, and it is responsible for bringing the majority of the region's annual rainfall between October and April. The regional circulation shifts associated with the ASM are part of a global-scale seasonal migration of the intertropical convergence zone (ITCZ) (Gadgil, 2018).

The ASM has a significant impact on the lives and well-being of a large proportion of the Australian population because of the importance of monsoon rains for sectors as diverse as agriculture and the shipping industry.

Writing – original draft:
Sarthak Mohanty, Christian Jakob, Martin S. Singh
Writing – review & editing:
Sarthak Mohanty, Christian Jakob, Martin S. Singh

Furthermore, by influencing regional-to-global circulation, the ASM plays a critical role in shaping both regional and global weather and climate patterns.

The effects of different scales on the variability of the Australian monsoon have been extensively documented (Allan, 1988; Berry & Reeder, 2016; Kajikawa et al., 2010; Kim et al., 2006; Kullgren & Kim, 2006; Lau et al., 2005; Lough, 1993; Mapes & Houze Jr, 1992, 1993; Narsey et al., 2017; Suppiah, 1992). Previous research on intra-seasonal to inter-annual variability has primarily focused on the Madden-Julian Oscillation (MJO), equatorial Rossby waves, mid-latitude fronts and waves, and El Niño Southern Oscillation (ENSO). While considerable effort has been made to understand the ASM in terms of its long-term climatological mean, there remain gaps in our knowledge regarding the underlying mechanisms controlling ASM variability.

To bridge these gaps, researchers have increasingly turned to advanced tools and models to simulate and predict the behavior of the ASM more accurately. General circulation models (GCMs), such as those used in the Coupled Model Intercomparison Project Phase 6 (CMIP6), are crucial for predicting Earth's climate. However, their coarse spatial resolution can lead to errors in modeling regional climate phenomena, including monsoons like the ASM (Dong & Dong, 2021; Grose et al., 2020; Li et al., 2023; Wang et al., 2020). Numerous studies have examined the performance of CMIP models in capturing the essential features of the ASM, focusing on both mean seasonal precipitation (Mohanty, Singh, & Jakob, 2024) and short-term precipitation bursts (Berry & Reeder, 2016; Mohanty, Jakob, & Singh, 2024; Mohanty et al., 2025; Narsey et al., 2017). These bursts are sequences of enhanced, persistent rainfall, typically lasting 2–5 days and affecting northern Australia's monsoon region, often driven by synoptic-scale systems such as monsoon lows or tropical disturbances (Narsey et al., 2018). These studies highlight the importance of accurately simulating both the seasonal mean and the sub-seasonal variability of the ASM to improve regional climate projections.

The shortcomings of CMIP6 models in accurately capturing the seasonal precipitation climatology of the ASM have already been highlighted in previous studies (Chung et al., 2023; Mohanty, Singh, & Jakob, 2024; Narsey et al., 2020). Discrepancies in how precipitation patterns are depicted can also introduce uncertainties in projecting future climate scenarios. The CMIP5 and CMIP6 models predict a wide range of changes in ASM precipitation by the end of the twenty-first century, with some models predicting a decrease and others predicting an increase (Brown et al., 2016; Narsey et al., 2020). While the range of future responses of ASM precipitation is reduced in the more recent CMIP6 ensemble compared to CMIP5, there is as yet no consensus on the sign of the change in ASM precipitation with warming.

In addition to the mean climate, short-term precipitation bursts are known to play a significant role in ASM dynamics. In a study utilizing CMIP5 models, Narsey et al. (2018) found a positive correlation between mean monsoon precipitation and the occurrence of bursts. However, most CMIP5 models displayed poor simulation of monsoon bursts, indicating the necessity for further investigation into this aspect. In this study, we aim to evaluate the capabilities of the most recent CMIP models (CMIP6) in simulating bursts, focusing on the vertically integrated Moist Static Energy (MSE) budget and using a methodology similar to that presented in Mohanty, Jakob, and Singh (2024).

To gain a thorough understanding of the impact of climate change on the ASM, it is necessary to investigate the mechanisms underlying changes in rainfall patterns in a warming world and the ability of models to reproduce them. We shift our focus in this study from assessing average ASM precipitation to a more nuanced examination of rainfall bursts. We exploit the methods developed in Mohanty, Jakob, and Singh (2024), which we have shown to provide a useful physically based assessment of monsoon behavior. Specifically, we examine the moist static energy budget and its evolution during monsoon bursts to understand the drivers of such bursts from an energetic perspective.

Previous studies have examined mean precipitation changes under global warming using the moisture budget (Seager et al., 2014; Sheng et al., 2023). Subsequent studies have suggested the decomposition of changes in precipitation into two primary mechanisms: thermodynamic and dynamic (Trenberth, 1999). The thermodynamic mechanism takes into account how changes in atmospheric moisture content caused by surface warming can result in changes in rainfall. The dynamic mechanism takes into account how changes in the circulation, especially changes in convergence, caused by warming can also result in changes in rainfall. Held and Soden (2006) have emphasized the importance of increased atmospheric moisture content due to surface warming in intensifying rainfall; for every degree Celsius increase in surface warming, the water vapor content in the atmosphere

Table 1
AMIP Models and Their Corresponding Source

Model	Source
BCC-CSM2-MR	Beijing Climate Center, China Meteorological Administration
CanESM5	Canadian Centre for Climate Modelling and Analysis
GFDL-CM4	Geophysical Fluid Dynamics Laboratory
IPSL-CM6A-LR	Institut Pierre-Simon Laplace
MPI-ESM-1-2-HR	Max Planck Institute for Meteorology (MPI-M)
MPI-ESM-1-2-LR	
CESM2	Community Earth System Model
MRI-ESM2-0	Meteorological Research Institute

increased by 7% (Allen & Ingram, 2002). The dynamic component, on the other hand, contributes positively in the tropics and negatively in the subtropics, depending heavily on the spatial distribution of climate forcing such as greenhouse gases versus aerosols (Emori & Brown, 2005; Pfahl et al., 2017; Shepherd, 2016; Trenberth et al., 2015). Here, we extend this previous body of work by applying the thermodynamic/dynamic decomposition to bursts rather than the overall mean rainfall. This allows for an analysis of changes in precipitation in terms of the weather systems, in this case monsoon bursts, that physically produce that precipitation.

The approach used here allows us to understand changes in ASM precipitation under warming in terms of the number of monsoon bursts, their strength, and the associated mechanisms identified through a thermodynamic/dynamic decomposition and through the moist static energy budget. We will then discuss how this information can help us understand how the ASM in the models behaves in a warming climate. We begin by describing the data and methodology in Section 2. Section 3 will be focused on the results, with Section 3.1 examining the mechanisms of burst evolution in models compared to reanalysis, and Section 3.2 describing their behavior in a warming scenario. Section 4 provides a discussion and draws the study's conclusions.

2. Data and Methodology

We utilize data from the European Centre for Medium-Range Weather Forecasts 5th generation reanalysis (ERA5) and AMIP simulations. ERA5 provides hourly temporal resolution, with a horizontal grid spacing of $0.25° \times 0.25°$ and 37 vertical pressure levels (Hersbach et al., 2020).

Additionally, we include eight CMIP6 AMIP simulations, selected based on the availability of variables needed for budget calculations (Table 1). Daily data from the first ensemble member of the AMIP experiments for each model are examined. We have calculated all budget terms in hourly resolution for ERA5 and then averaged them daily. We have directly computed the terms at daily resolution for CMIP6 data. We note that computing MSE budgets from daily mean fields in CMIP models may omit contributions from sub-daily, high-frequency disturbances (e.g., easterly waves) to horizontal advection, as shown in previous studies of the ITCZ and MJO (Maloney, 2009; Peters et al., 2008). In this study, however, our focus on multi-day burst evolution and composite-based analyses of monsoon bursts, together with the consistent use of daily averages across data sets, suggests that such effects are likely secondary. Nonetheless, future work with higher temporal resolution data could further refine these estimates. Furthermore, using only eight common pressure levels for vertical integration in both ERA5 and CMIP6 data may introduce uncertainties in the MSE budget closure, particularly affecting the accuracy of the vertically integrated horizontal MSE advection. While the vertical advection term, a small residual of large moisture import and dry static energy export terms, may also be affected, its contribution is secondary in our analyses. We account for these uncertainties by interpreting the residual in the MSE budget, though future analyses with finer vertical resolution could improve accuracy. All analyses are performed on the native horizontal grid of each model and reanalysis, using only the common eight pressure levels. Certain models as well as ERA5 provide data at pressure levels that fall below the orography and hence exceed the surface pressure. To address this, we have used a topography criterion on both reanalysis and CMIP6 data. This means that we have only considered pressure levels less than or equal to the surface pressure in evaluating vertically integrated quantities.

We define Australian monsoon bursts in both the CMIP6 models and reanalysis using the method described by Berry et al. (2012) and outlined below. Our focus is on the Australian monsoon region (11°S–18°S, 125°E–145°E). The analysis period spans 1983 to 2014.

First, we compute a climatology of the mean and standard deviation of daily precipitation throughout the year. This climatology time series is then smoothed using a 60-day low-pass filter (Fourier transform retaining the first six harmonics), producing a smoothed time series representing the seasonal rainfall climatology. Similarly, a smoothed time series of rainfall standard deviation is generated, representing the seasonal climatology of rainfall variability.

Burst events are identified when the daily rainfall, averaged over the monsoon region, increases from below a lower threshold of $\mathrm{P}_{clim} - 0.5\sigma_{clim}$ to above an upper threshold of $\mathrm{P}_{clim} + 0.5\ \sigma_{clim}$ within 7 days. This threshold choice follows earlier studies (Berry & Reeder, 2016; Mohanty, Jakob, & Singh, 2024; Narsey et al., 2017) and provides a balance between capturing dynamically meaningful deviations from the seasonal climatology and avoiding spurious detection of minor fluctuations. The $+0.5\ \sigma_{clim}$ range has been shown in these studies to robustly identify transitions between suppressed and active phases of the monsoon. Here, P_{clim} and σ_{clim} denote the seasonal climatologies of rainfall and its standard deviation, respectively. The first day of the burst event is marked by the rainfall exceeding the upper threshold. Importantly, burst detection and analysis are confined to the rainy season, from October to April.

Our goal, as in Mohanty, Jakob, and Singh (2024), is to link the evolution of rainfall bursts to the moist static energy budget. To accomplish this, we calculate all budget terms over a 15-day period, beginning 7 days before and ending 7 days after the start date of each burst.

The column-integrated MSE budget equation for a single location can be approximately expressed as follows (Hill et al., 2017, 2018; J. Neelin & Held, 1987):

$$\frac{\partial\{h\}}{\partial t} + \nabla\cdot\{h\vec{v}_h\} = L_vE + H + R_t + R_s\cdot \tag{1}$$

MSE is defined as $h = c_pT + gz + L_vq$, where c_p is the specific heat capacity at constant pressure, T is the temperature, z is the geopotential height, and q is the specific humidity. The terms L_vE, H, R_t, and R_s represent the latent heat flux (LHF), sensible heat flux (SHF), and net radiation at the top of the atmosphere and the surface, respectively. The curly brackets denote the column mass integral, defined as $\{\cdot\} = \int_0^{p_s}(\cdot)\ dp/g$, where p_s is the surface pressure and g is the gravitational acceleration. The first term on the left-hand side, $\partial_t\{h\}$, signifies the rate of change in vertically integrated MSE over time (moist enthalpy),which we denote the storage term. The second term, $\nabla\cdot\{h\vec{v}_h\}$, represents the convergence or divergence of MSE flux within the column and can be calculated by adding its vertical and horizontal advection terms. This can be expressed as:

$$\nabla\cdot\{h\vec{v}_h\} = \{\omega\partial_p h\} + \{\vec{v}_h\cdot\nabla h\}, \tag{2}$$

where ω denotes the vertical velocity in pressure coordinates. Alternatively, the divergence can be calculated by adding the MSE flux from each boundary and applying a mass correction, similar to the method used in the study by Mohanty, Singh, and Jakob (2024) and Inoue and Back (2015). The right-hand side of Equation 1 is collectively referred to as the Net Energetic Forcing (NEF). Since temperature gradients are weak in the tropics, the moist enthalpy can be approximated by the moisture tendency (Mohanty, Jakob, & Singh, 2024). This approximation allows us to rewrite Equation 1 as follows:

$$\frac{\partial\{L_vq\}}{\partial t} + \nabla\cdot\{h\vec{v}_h\} = L_vE + H + R_t + R_s, \tag{3}$$

Two important quantities arise in the moist static energy budget framework that characterize the amplification and decay of column humidity: the gross moist stability (GMS) and the drying efficiency (DEF). Introduced by J. Neelin and Held (1987) The GMS represents the efficiency with which divergent circulations export energy.

In addition to analyzing the MSE budget, we applied the concept of GMS-based DEF from Mohanty, Jakob, and Singh (2024) and Inoue and Back (2015) to investigate bursts in the model output. GMS serves as a metric to link circulation and convection, originally introduced by J. Neelin and Held (1987). For this study, we adopted the definition provided by Raymond et al. (2009), which can be expressed as:

$$\tau = \frac{\nabla \cdot \{h\vec{v}_h\}}{\nabla \cdot \{s\vec{v}_h\}}, \tag{4}$$

The drying efficiency was introduced by Inoue and Back (2015) and used in Mohanty, Jakob, and Singh (2024) to represent the growth and decay of column moisture anomalies. The DEF can be computed by calculating GMS (τ) and a critical GMS (τ_c) and taking their difference. The critical GMS is defined as:

$$\tau_c = \frac{L_v E + H + R_t + R_s}{\nabla \cdot \{s\vec{v}_h\}} = \frac{\mathrm{NEF}}{\nabla \cdot \{s\vec{v}_h\}}, \tag{5}$$

The DEF is may then be expressed as:

$$\mathrm{DEF} = \tau - \tau_c = \frac{\nabla \cdot \{h\vec{v}_h\} - \mathrm{NEF}}{\nabla \cdot \{s\vec{v}_h\}} \approx \frac{-\partial\{L_v q\}/\partial t}{\nabla \cdot \{s\vec{v}_h\}}, \tag{6}$$

where $\nabla \cdot \{s\vec{v}_h\}$ denotes the net divergence of dry static energy (DSE), defined as $s = c_p T + gz$. From (Equation 6) we see that DEF expresses the normalized rate of drying by the atmosphere through a combination of the large-scale circulation and local energetic forcing terms. The DEF is crucial in identifying different phases of convection in a convectively active atmosphere ($\nabla \cdot \{s\vec{v}_h\} > 0$).

In the next section, we will use the above MSE-based diagnostics to compare the behavior of rainy season bursts in ERA5 with those in the model's AMIP simulations.

3. Results

We begin by comparing bursts in models to ERA5. To do so, we employ the MSE budget approach developed by Mohanty, Jakob, and Singh (2024), as it provides insights into the mechanisms for burst amplification and decay. One of our goals is to investigate whether there is a connection between a model's ability to simulate the MSE evolution of rainfall bursts and its overall simulation of ASM rainfall as well as the behavior of the model in a warmer climate. Section 3.1 will focus on model evaluation, while Section 3.2 will look at how the models behave in a warming scenario.

3.1. The Fidelity of CMIP6 Models in Depicting the Rainfall Burst Evolution

3.1.1. Monsoon Precipitation and Number of Bursts

The average precipitation during the extended summer monsoon months (October–April) from 1983 to 2014, as produced by ERA5, is 5 mm/day, with a total of 178 burst events recorded over the entire period (1983–2014). Upon comparing these values with the 8 AMIP CMIP6 outputs, it is evident that there exists significant variation among models with respect to both average precipitation and the number of bursts (Figure 1). This finding is consistent with the study conducted by Narsey et al. (2020), wherein certain models (MPI-ESM-1-2-LR, MPI-ESM-1-2-HR) demonstrate anomalously low precipitation while others (CanESM5, BCC-CSM2-MR, IPSL-CM6A-LR, CESM2) exhibit anomalously high precipitation compared to reanalysis. In contrast, the MRI-ESM2-0 and GFDL-CM4 models show average precipitation rates of 5.0 and 4.9 mm/day, respectively, aligning closely with ERA5.

Across models, the number of bursts and the mean precipitation exhibit a statistically significant positive correlation ($r = 0.79$, $p < 0.05$), indicating that wetter models generally simulate more burst events. In the observations (ERA5), this relationship is inherently represented by a single point; however, the modeled intercomparison suggests that higher mean rainfall is systematically associated with more frequent burst activity. Among the eight models, four underestimate both mean precipitation and burst frequency, while three (IPSL-CM6A-LR, BCC-CSM2-MR and CESM2) overestimate both. Interestingly, CanESM5 stands out as an exception—it overestimates mean precipitation but underestimates the number of bursts. This mismatch suggests that CanESM5 tends to produce excessively continuous rainfall rather than discrete high-intensity events, leading to poor representation of

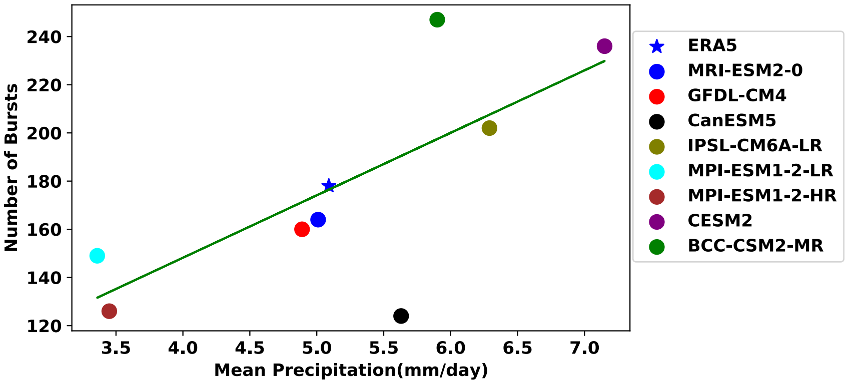

Figure 1. Total number of bursts during the period 1983–2014 plotted against mean precipitation over the summer monsoon months (October–April) in the monsoon region and the number of bursts for both reanalysis and CMIP6 models.

the observed burst–mean precipitation relationship. A summary of mean precipitation and burst counts for all models is provided in Table 2.

The time evolution of precipitation bursts is important because it can reveal the physical processes that cause these events. Composites of burst precipitation from 7 days before burst onset to 7 days after are shown for both models and reanalysis in Figure 2. In all cases, precipitation begins to increase at day −7, peaking around day 0 or day +1, and then decreasing. The magnitude and evolution of ERA5 and the climate models are similar, with ERA5 peaking around day +1. During the amplification phase, the climate models exhibit a similar evolution but differ during the decay phase. Some models, like CESM2 and BCC-CSM2-MR, show an abrupt decay, whereas others, like MRI-ESM2-0, MPI, and, IPSL-CM6A-LR, show a gradual decay, similar to ERA5. In contrast, CanESM5 and GFDL-CM4 exhibit an intermediate behavior, neither distinctly abrupt nor gradual.

These differences in the decay phase of precipitation bursts suggest that climate models may be misrepresenting the physical processes that cause these events. The next section will focus on comparing the processes associated with the bursts. First, we will apply the MSE budget analysis described in Section 2.

3.1.2. Time Evolution of MSE Budget and Drying Efficiency

To explore various factors influencing precipitation evolution, akin to Mohanty, Jakob, and Singh (2024), we compute the MSE budget averaged over northern Australia. Taking the spatial mean of Equation 3, we have

Table 2
Comparison of Model Performance Against ERA5 Reanalysis Across Precipitation, Burst Characteristics, and Key MSE Budget Terms

Model	Mean precipitation (mm/day)	No. of bursts	$[\nabla\cdot\{h\vec{v}_h\}]$ (RMSE) (W/m^2)	$\gamma[\nabla\cdot\{s\vec{v}\}]+\beta$ (RMSE) (W/m^2)	$[\{\vec{v}_h\cdot\nabla L_v q\}]$ RMSE (W/m^2)	$[\vec{v}_h\cdot\nabla L_v q]$ (RMSE) (vertical profile) (1000-100 hpa) (J/sec)	Frequency in cluster RMSE (%)	Rank
ERA5	5.0	178	0	0	0	0	0	
GFDL-CM4	4.9	160	13	5	18	0.004	9	1
MRI-ESM2-0	5.0	164	15	7	16	0.003	10	2
CanESM5	5.6	124	17	6	26	0.004	12	3
IPSL-CM6A-LR	6.3	202	25	8	26	0.003	11	4
MPI-ESM-1-2-LR	3.4	149	15	6	28	0.005	13	5
MPI-ESM-1-2-HR	3.5	126	28	6	26	0.005	18	6
BCC-CSM2-MR	5.9	247	33	18	35	0.006	13	7
CESM2	7.2	236	51	30	28	0.004	17	8

Note. Lower RMSE values indicate closer agreement with reanalysis.

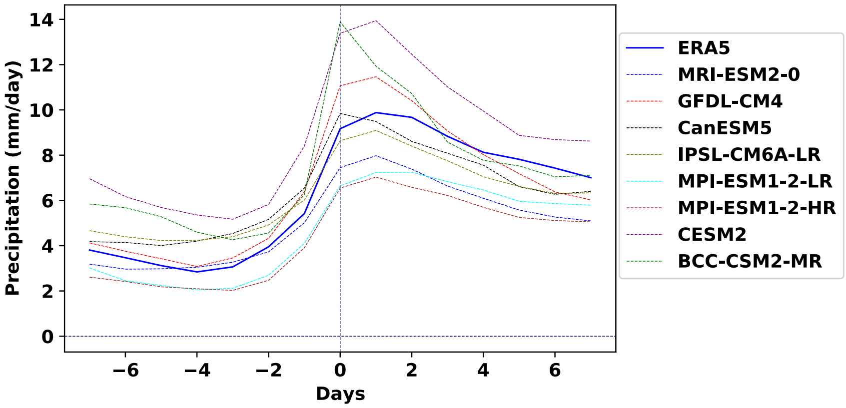

Figure 2. Temporal evolution of precipitation burst composite (mm/day) for ERA5 and climate models. ERA5 is highlighted with thick blue line, while other models are represented with dashed lines.

$$\frac{\partial[\{L_v q\}]}{\partial t} + [\nabla \cdot \{h\vec{v}\}] = [\mathrm{NEF}], \tag{7}$$

where the square brackets represent an average over the Australian monsoon region defined by the latitude-longitude box (11°S–18°S, 125°E–145°E). We use the divergence theorem to express the second term on the left-hand side in terms of the horizontal velocity over the region's boundary. This term is then evaluated after adding a height independent correction to the velocity field to ensure the numerical integration satisfied conservation of mass (Hill et al., 2017; Mohanty, 2024; Mohanty, Singh, & Jakob, 2024). To understand the evolution of the budget (Equation 7), we further consider the approach of Inoue and Back (2015). Inoue and Back (2015) have shown that the relationship between the NEF and $[\nabla \cdot \{s\vec{v}\}]$ can be characterized by a first-order linear regression, which can be expressed as $[\mathrm{NEF}] = \gamma[\nabla \cdot \{s\vec{v}\}] + \beta$, where γ and β correspond to the slope and intercept respectively. We adopt this regression for two reasons: (1) although NEF is strongly related to DSE divergence, the relationship is not perfectly linear and some outliers exist; the regression provides a physically interpretable approximation that minimizes the influence of these outliers; and (2) the regression reduces the dimensionality of the budget by consolidating multiple forcing terms into a single relation with DSE divergence, thereby clarifying the contribution of MSE divergence to burst evolution without tracking each flux term individually. By applying the above concept, Equation 3 can be written as;

$$\frac{\partial[\{L_v q\}]}{\partial t} = (\gamma[\nabla \cdot \{s\vec{v}\}] + \beta) - [\nabla \cdot \{h\vec{v}\}]\cdot \tag{8}$$

Figure 3 shows the different terms of Equation 8 for ERA5 and the eight AMIP simulations from 7 days before to 7 days after a rainfall burst. Similar to Mohanty, Jakob, and Singh (2024), we find that in the reanalysis, the time evolution of the budget is strongly related to that of the MSE divergence. A quantitative analysis based on relative weight analysis (Tonidandel & LeBreton, 2011) supports these findings, demonstrating that the MSE divergence contributes roughly 90%, to the overall temporal evolution of $(\gamma[\nabla \cdot \{s\vec{v}\}] + \beta) - [\nabla \cdot \{h\vec{v}\}]$ whereas $(\gamma[\nabla \cdot \{s\vec{v}\}] + \beta)$ contributes less than 10%. We also find that the linear approximation described generally allows for the budget to approximately close across the burst life-cycle (compare the blue lines and dashed olive lines in Figure 3). However, there are exceptions to this in some models, in particular the IPSL-CM6A-LR and BCC-CSM2-MR models. We note that the residual between the two terms——represented by the difference between the thick blue and dashed olive lines in Figure 3—also partly reflects errors introduced by numerical computation of the terms involved on a finite number of pressure levels (Seager & Henderson, 2013).

An advantage of the decomposition of the budget as performed in Figure 3 is that it strongly relates to the definition of a key MSE-analysis quantity, the DEF defined in Equation 6. In convectively active regions where $[\nabla \cdot \{s\vec{v}\}] \geq 0$, the sign of moisture tendency (or negative of DEF) determines the convection phase: positive values imply growth and an amplification of humidity anomalies, whereas negative values indicate decay. Figure 3 shows that the DSE divergence term remains positive throughout the burst periods. Most models and reanalysis

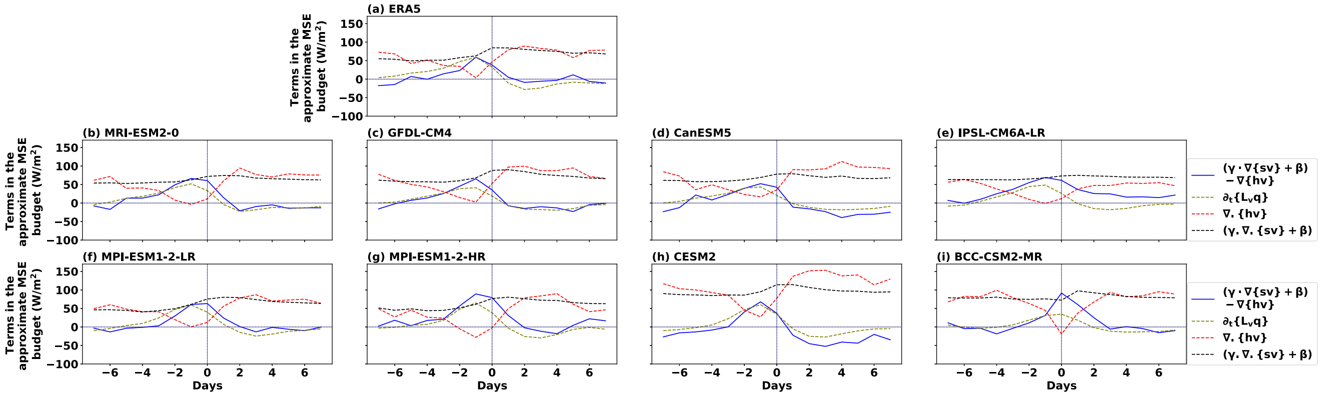

Figure 3. Terms in the approximate MSE budget (Equation 8)—namely $(\gamma[\nabla\cdot\{s\vec{v}\}] + \beta) - [\nabla\cdot\{h\vec{v}\}]$, storage, $[\nabla\cdot\{h\vec{v}\}]$, and $\gamma[\nabla\cdot\{s\vec{v}\}] + \beta$—are indicated by thick blue, dashed olive, dashed red, and dashed black lines, respectively.

show a growth phase prior to the burst peak, followed by a weaker decay phase. Once again, the IPSL-CM6A-LR and BCC-CSM2-MR models are notable outliers. The IPSL-CM6A-LR model shows a negative DEF that decays after the burst peak, similar to how precipitation evolves (Figure 2). Convection does not gradually grow prior to day 0 of the rainfall burst in the BCC-CSM2-MR model, and unlike in reanalysis, the growth phase lasts for about a day after day 0 before decaying. This is not observed in precipitation, which starts to fall after reaching its peak on day 0 (green dotted line in Figure 2).

To quantitatively evaluate the performance of the models in comparison to the reanalysis, we calculated the RMSE between the models and the reanalysis for the MSE divergence and $(\gamma[\nabla\cdot\{s\vec{v}\}] + \beta)$. For MSE divergence, the GFDL-CM4, MRI-ESM2-0, and MPI-ESM-1-2-LR models all agree well with ERA5 with low RMSE, indicating that they can capture the overall temporal evolution of the bursts. The CESM2, MPI-ESM-1-2-HR, and BCC-CSM2-MR models, on the other hand, deviate the most from ERA5, indicating a challenge in accurately representing MSE divergence dynamics.

The $\gamma[\nabla\cdot\{s\vec{v}\}] + \beta$ component shows varying levels of agreement with ERA5. The GFDL-CM4 model effectively reproduces the time evolution of this term in ERA5, demonstrating its ability to capture related processes. However, BCC-CSM2-MR and CESM2 deviate significantly from ERA5, indicating potential flaws in representing the dynamics of this component in this model. The results are summarized in columns 4 and 5 of Table 2.

3.1.3. Decomposition of MSE Divergence

In the next step, we decompose the MSE divergence into horizontal and vertical advection terms using the continuity equation in pressure coordinates (Equation 9) as follows:

$$[\nabla\cdot\{h\vec{v}\}] = [\{\omega\partial_p h\}] + [\{\vec{v}\cdot\nabla h\}]\cdot \tag{9}$$

This decomposition is necessary to understand the behavior of bursts in models. As highlighted by Mohanty, Jakob, and Singh (2024), the horizontal advection of MSE, particularly moisture, plays a crucial role in governing the overall temporal evolution of MSE divergence during ASM rainfall bursts.

As discussed in Mohanty, Jakob, and Singh (2024), the advection values on the right-hand side cannot be calculated simply by adding the boundary values, nor can we apply the mass budget correction performed for the full divergence. Therefore, we have used the uncorrected wind from each model to calculate these advection terms. We find that this does not affect our main conclusions. The decomposition is applied to all bursts individually and then averaged to produce the composite, which is summarized in Figure 4. MSE divergence, horizontal MSE advection, and vertical MSE advection are denoted by thick blue, dashed red, and dashed black lines, respectively. To emphasize the critical role of moisture, the figure also shows its contribution to horizontal moisture advection (dotted dashed purple). Figure 4a shows ERA5, whereas Figures 4b–4i show the model output.

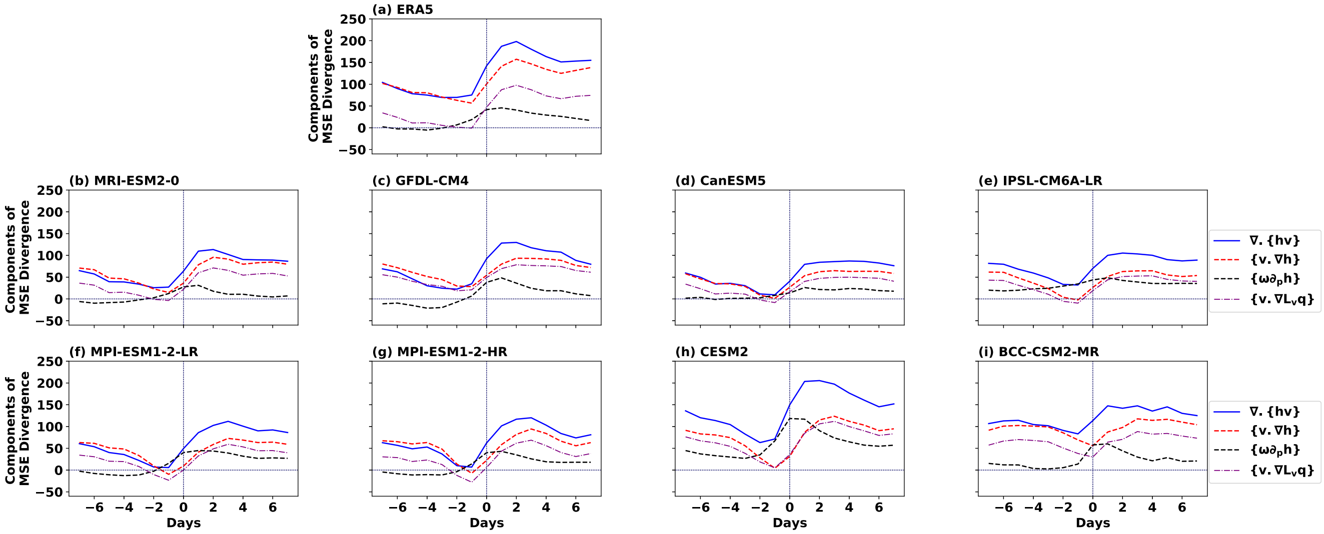

Figure 4. MSE divergence and its components for ASM rainfall bursts. The figure shows MSE divergence (solid blue), horizontal MSE advection (dashed red), and vertical MSE advection (dashed black). The purple dashed line denotes the contribution from moisture to the horizontal advection of MSE.

In ERA5, we found that changes in horizontal MSE advection have the greatest influence on the temporal evolution of MSE divergence (compare the thick blue and dashed red lines in Figure 4a). This result is consistent with prior studies of the MSE budget in the context of the MJO and boreal summer ISO (Adames & Kim, 2016; Jiang et al., 2018), though our analysis is more phenomenon- and timescale-agnostic. During this pre-burst period, the weakened horizontal export of MSE, together with enhanced surface latent and sensible heat fluxes, contributes to a gradual moistening of the lower troposphere. This accumulation of moisture and energy preconditions the atmosphere for the subsequent amplification of convection, consistent with previous studies showing that the intensification of precipitation is closely associated with increases in precipitable water (Mohanty, Jakob, & Singh, 2024).

Vertical advection, on the other hand, is near zero at the start of the burst, with a peak around day 0. The divergence and horizontal advection of MSE sharply increase after day 0, while the vertical advection of MSE declines (indicated by the dashed black line). Although vertical advection has little effect on the temporal evolution of MSE divergence, it has an effect on its magnitude, especially during the peak and decay phases. MSE divergence of higher magnitude indicates a higher MSE export from the system, associated with a top-heavy ascent profile and deep convection (Bui et al., 2016). Finally, this results in convective decay and a decrease in precipitation (Inoue & Back, 2015; Mohanty, Jakob, & Singh, 2024). Next, we investigate the models' ability to reproduce the temporal behavior of MSE divergence and its relationship with horizontal MSE advection.

When assessing the MSE divergence evolution in the models we find that while horizontal MSE advection influences bursts in the same way that it does in ERA5 (evolution during the convectively amplification/decay), it is not always the primary contributor to the temporal evolution of MSE divergence. Notably, the impact of vertical MSE advection is overestimated in some models such as CESM2 and BCC-CSM2-MR. Between horizontal and vertical contributions to MSE divergence, CESM2 and BCC-CSM2-MR assign excessive weight to the vertical term, which produces steeper amplification and faster decay of convection. This bias manifests in the abrupt rise and fall of precipitation in both models (Figure 2), consistent with their overestimation of vertical advection. The contrast becomes clearer when examining the vertical velocity structures (Figure 5). In these plots, the blue line marks the mean vertical motion across the full period (−7 to +7 days), while the red and olive lines highlight the accumulation (−7 to −1 days) and peak/decay (0 to +7 days) phases, respectively.

In ERA5 (Figure 5a), ascent during the accumulation phase (red line) is weak and temporally confined (limited red spreading), which leads to negative column-integrated vertical MSE advection prior to the peak (dashed black line in Figure 4). This indicates that the vertical term plays only a minor role in the buildup. After the peak (olive line), ascent strengthens across levels but remains relatively narrow (limited olive spreading), producing a gradual decline in column-integrated vertical MSE advection and a smoother temporal transition (Figure 2). Importantly,

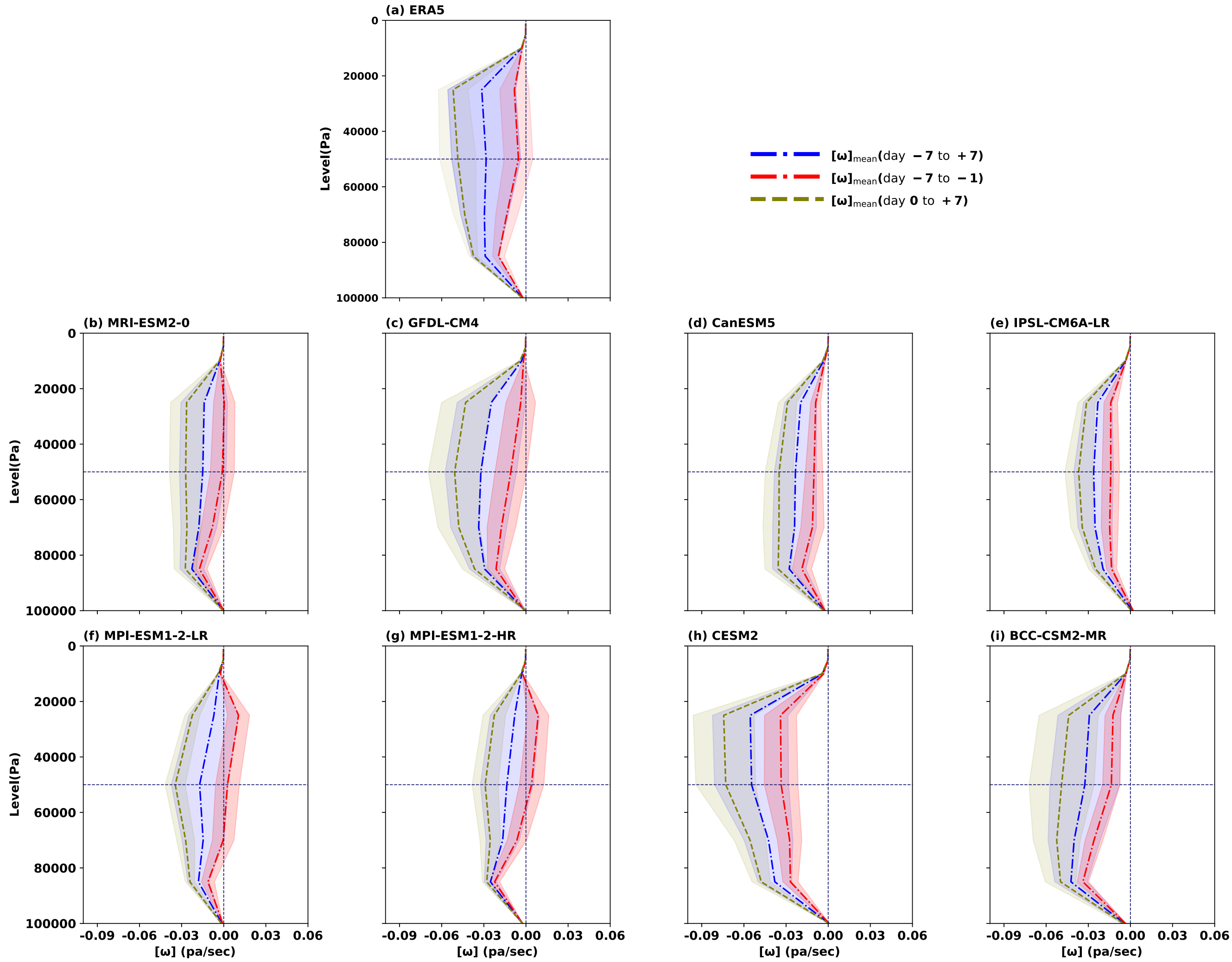

Figure 5. Vertical profile of vertical velocity. Blue dash–dot: mean over days −7 to +7 (shaded band = ±1 SD). Red dash–dot: mean over days −7 to −1 (shaded band = ±1 SD). Olive dashed: mean over days 0 to +7 (shaded band = ±1 SD).

the overall column-integrated magnitude in ERA5 remains low, so the vertical advection term contributes less to the total MSE budget compared to the horizontal component.

In CESM2 and BCC-CSM2-MR, by contrast, both the magnitude and vertical extent of ascent are much larger. During −7 to −1 days, strong, vertically extensive ascent—especially in CESM2 (see the dashed red line in Figure 5h)—leads to near-zero or even positive column-integrated vertical MSE advection prior to the peak. This early enhancement amplifies the role of the vertical term relative to ERA5. After the peak, ascent intensifies and, because it spreads broadly across the column (greater olive spreading), both the buildup and subsequent decline occur much more rapidly. This combination drives the sharp post-peak drop in vertical MSE advection (Figure 4). In comparison, the other models exhibit weaker pre-peak ascent (dashed red line) and comparatively weaker post-peak profiles than CESM2 (less difference between olive and red), aligning more closely with ERA5 and producing a smoother and weaker temporal evolution of vertical MSE advection. The overestimation in CESM2 alters the equilibrium between horizontal and vertical contributions to MSE divergence, resulting in steeper amplification and decay of convection in both models. The abrupt rise and fall of precipitation in CESM2 and BCC-CSM2-MR (Figure 2) are consistent with this excessive influence of vertical advection. These behaviors indicate that both models misrepresent the vertical structure of convective processes, reducing their ability to reproduce the smoother transitions seen in reanalysis.

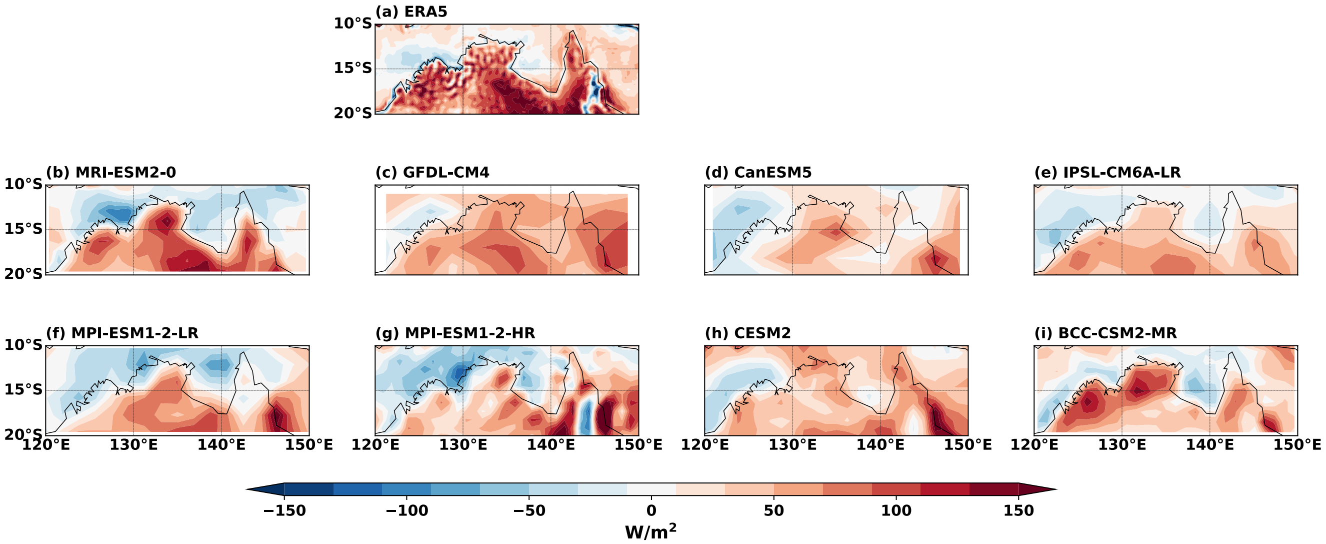

Figure 6. Spatial diagram of horizontal moisture advection for reanalysis and model output.

The temporal evolution of MSE divergence has correlation coefficients of 0.8 or higher with horizontal MSE advection in all models except the above two. The temporal evolution of horizontal MSE advection in ERA5 is primarily caused by its moisture component (purple line in Figure 4). In our analysis, the difference between the horizontal MSE and moisture advection terms primarily arises from horizontal DSE advection. Under the weak temperature gradient approximation, horizontal temperature advection in the tropical free troposphere is generally small (Charney, 1969; Inoue et al., 2021; Sobel et al., 2001). In our simulations, the DSE horizontal advection term remains relatively small in magnitude but exhibits a consistent, non-zero contribution that accounts for the offset between horizontal MSE and moisture advection. This steady background DSE horizontal advection influences the mean level of MSE horizontal advection, while the variability in MSE during burst events is largely governed by changes in horizontal moisture advection, consistent with Mohanty, Jakob, and Singh (2024).

To understand the horizontal moisture advection in detail, we have plotted its spatial distribution over the northern Australian tropics (Figure 6). At day 0, when convection peaks, ERA5 shows strong horizontal moisture export (red shading) over the continental regions of northern Australia, while import (blue shading) dominates over the adjacent ocean, particularly in the western sector; the remaining ocean areas exhibit only weak export (Figure 6a). Although the region as a whole exhibits net horizontal moisture export, this export remains smaller than the net NEF, leading to an overall amplification of convection on day 0 (see Figure 3a). This land–ocean contrast reflects the import of oceanic moisture into the monsoon trough. Among the models, MRI-ESM2-0 most closely resembles ERA5, capturing both the amplitude and the placement of land-based export, although its oceanic import is more spatially extensive than in ERA5. GFDL-CM4 reproduces the basic contrast but extends the export region too broadly across land, while CanESM5 produces a weaker magnitude of export over land even though its oceanic structure is similar to ERA5. IPSL-CM6A-LR also retains the ERA5-like pattern but with systematically reduced magnitudes in both export and import. The MPI models broadly capture the observed contrast but tend to exaggerate the import signal over land or stretch it into regions where ERA5 shows export. CESM2 reproduces the broad pattern with high fidelity in the sign of import versus export, yet its strongest export centers are misplaced and overly localized, giving rise to both visually intense red patches and an overall underestimation of export across ERA5-exporting grid points. BCC-CSM2-MR likewise generates strong export over land, but the grid-level placement of these export regions differs substantially from ERA5, and at the same time its import over the oceans is muted. This misrepresentation of the land–ocean distribution of horizontal advection in CESM2 and BCC-CSM2-MR is consistent with their tendency to overstate vertical MSE advection and to simulate an overly abrupt rise and decay of convection, in contrast to the smoother transitions found in ERA5.

We find that all models qualitatively reproduce this behavior quite well. When calculating the RMSE of the simulated horizontal moisture advection, as we did in the previous section for MSE divergence, we find that the

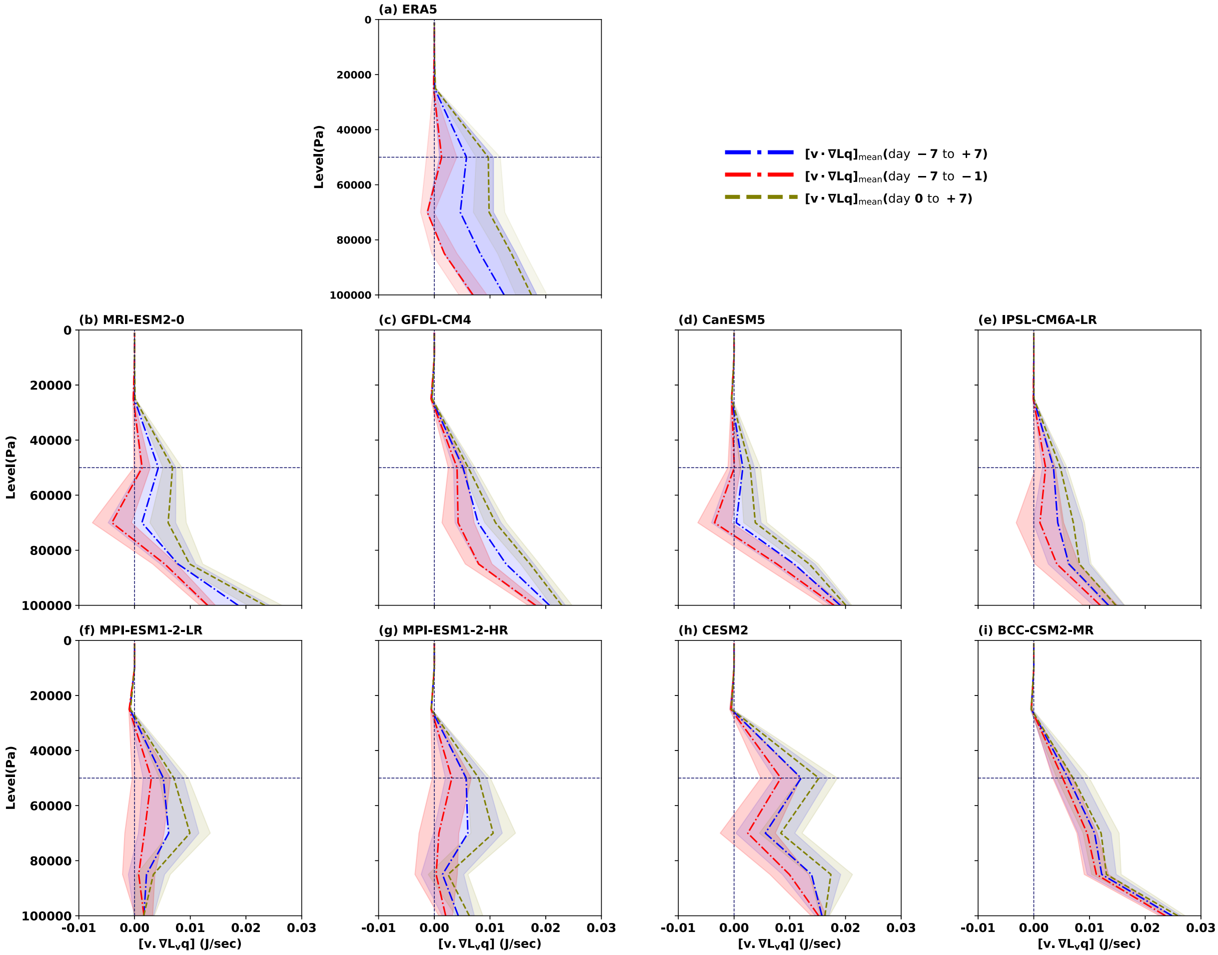

Figure 7. Vertical profile of horizontal moisture advection. Blue dash–dot: mean over days −7 to +7 (shaded band = ±1 SD). Red dash–dot: mean over days −7 to −1 (shaded band = ±1 SD). Olive dashed: mean over days 0 to +7 (shaded band = ±1 SD).

MRI-ESM2-0 has the lowest RMSE values when compared to ERA5. The BCC-CSM2-MR model, on the other hand, deviates the most from ERA5. The RMSE values are summarized in the sixth column of Table 2.

3.1.4. Vertical Profile of Horizontal Moisture Advection

Given the importance of horizontal moisture advection in the MSE evolution of ASM rainfall bursts, it is worth investigating the vertical structure of moisture advection to enhance our understanding of its impact on the temporal evolution of MSE divergence and test the ability of the models to reproduce the vertical integrals with the correct vertical structure. To quantify the variability of horizontal moisture advection, calculations were performed at each pressure level for a composite spanning 7 days before and 7 days after day 0 of the burst event. The results, presented in Figure 7, highlight three perspectives: the mean over the full 15-day window (days −7 to +7; blue dash–dot), the mean for the pre-burst period (days −7 to −1; red dash–dot), and the mean for the post-burst period (days 0 to +7; olive dashed). In each case, the shaded envelope around the mean curve indicates the corresponding standard deviation, reflecting the spread across the individual monsoon bursts.

When comparing with ERA5 (Figure 7a), it is evident that models differ in terms of the vertical structure of moisture advection (particularly in the lower troposphere), despite having similar magnitude and variation in column-integrated horizontal moisture advection (Figure 4a). In ERA5 (Figure 7a), the vertical profile of horizontal moisture advection decreases from the surface up to roughly 700 hPa, rises to a weak maximum near 500 hPa, and then falls off aloft. The pre-burst (red) curve lies consistently to the left of the 15-day composite mean (dashed blue), while the post-burst (olive) curve lies to the right, giving the clear ordering red < blue < olive. This ordering indicates weaker horizontal moisture export before burst onset and stronger export after Day 0, with the largest differences between the post-burst and pre-burst (see olive vs. red) phases occurring in the lower troposphere and the curves converge near 500–600 hPa.

MRI-ESM2-0 (Figure 7b) reproduces this ERA5 behavior most faithfully, capturing both the vertical structure and the monotonic progression from the pre-burst period through the full 15-day composite to the post-burst period seen in the reanalysis, with the largest differences confined to the lower troposphere and moisture import at mid levels. IPSL-CM6A-LR (Figure 7e) also captures the overall shape and ordering, although its red and olive curves are more tightly clustered than ERA5, indicating a muted amplitude of the pre- to post-burst change. GFDL-CM4 (Figure 7c) and CanESM5 (Figure 7d) preserve the general mid-tropospheric structure but tend to understate the red–olive separation: both show a similar slope with height to ERA5 but smaller phase contrast, and CanESM5 in particular is displaced toward larger magnitudes while keeping the pre/post curves relatively close to one another.

The two MPI configurations (Figures 7f and 7g) do not reproduce the ERA5 near-surface behavior. At 1,000 hPa MPI departs from the characteristic ERA5 decrease toward 700 hPa; instead, the MPI profiles show a different near-surface magnitude/shape (a noticeable offset or plateau at 1,000 hPa) that prevents a faithful replication of the ERA5 phase-dependent ordering in the lowest levels. Although the MPI-ESM-1-2-HR run is marginally closer to ERA5 than the LR configuration at some mid-levels, neither MPI version captures the ERA5 near-surface decrease cleanly, and both exhibit reduced convergence with ERA5 in the lower troposphere.

CESM2 (Figure 7h) exhibits a systematic positive bias in horizontal moisture advection compared to ERA5. At nearly all pressure levels, both the pre-burst (red) and post-burst (olive) profiles are shifted to the right of the corresponding ERA5 curves, indicating stronger moisture export in both phases. The bias is most pronounced in the lower troposphere, from the surface up to about 700–850 hPa, where CESM2 substantially overestimates export relative to ERA5. Although the model maintains the expected ordering of red < dashed blue < olive, the entire set of profiles is displaced toward larger values, so the difference between pre- and post-burst phases occurs on top of a baseline overestimation. With height, the bias gradually diminishes: in the mid-troposphere (500–600 hPa) the separation between CESM2 and ERA5 narrows, and in the upper troposphere (above 400 hPa) the curves converge closely. This behavior shows that CESM2 does not simply amplify the Day-0 transition, but instead produces consistently stronger horizontal moisture export before and after bursts, with the largest errors confined to the lower troposphere. BCC-CSM2-MR (Figure 7i) departs most strongly from ERA5: its entire column is shifted toward larger advection magnitudes, its mid-level curvature differs from ERA5, and the pre-to-post-phase separation is inconsistent with the coherent phase evolution observed in ERA5 (with occasional level-by-level crossings). These departures explain BCC-CSM2-MR's relatively large RMSE.

Overall, ERA5 displays a robust pre- to post-burst pattern (weaker export before, stronger after) with greatest differences in the lower troposphere and import near mid-levels. MRI-ESM2-0 and IPSL-CM6A-LR come closest to reproducing both the vertical shape and the phase-dependent ordering, several models capture the shape but mute the phase contrast, CESM2 amplifies it, and MPI (both LR and HR) and BCC-CSM2-MR show notable low-level mismatches—with MPI specifically failing to reproduce ERA5's near-surface behavior around 1,000 hPa.

The RMSE is computed by comparing each reanalysis with each model, considering all eight models within a 7-day window before and after day 0. In summary, both the quantitative RMSE analysis and the qualitative vertical profile examination in Figure 7 provide insights into the performance of different models compared to the reanalysis. Lower RMSE values are found in the MRI-ESM2-0 and IPSL-CM6A-LR models, indicating better agreement with the reanalysis data. Furthermore, with varying degrees of fidelity, the vertical profiles of these models resemble the reanalysis. In contrast, the BCC-CSM2-MR model has higher RMSE values and significant differences in the vertical profile compared to the reanalysis. Results for the RMSE of the vertical profiles are summarized in the 7th column of Table 2.

3.1.5. Model Evaluation of Burst Types

In Mohanty, Jakob, and Singh (2024), the authors observed significant variability in the temporal evolution of ASM rainfall bursts. Hence, in addition to performing the composite analyses above it is important to investigate whether the models are able to capture the variations between bursts. To address the issue, we extended our investigation, following a similar approach to Mohanty, Jakob, and Singh (2024), by incorporating a cluster analysis. We identified three main burst types each with its unique characteristics. To compute the clusters, we applied a k-means clustering analysis on the divergences of moist and dry static energy $[\nabla \cdot \{h\vec{v}\}]$ and $[\nabla \cdot \{s\vec{v}\}]$. These terms were used as they corresponded to the axes of the GMS plane defined by Inoue and Back (2015), who also showed that precipitation events in the tropics followed a characteristic path through the GMS plane. Mohanty, Jakob, and Singh (2024) considered the 15 days time evolution (-7 to $+7$ days) of $[\nabla \cdot \{h\vec{v}\}]$ and $[\nabla \cdot \{s\vec{v}\}]$ during bursts as elements in a 30 dimension vector space. k-means clustering was then used to define clusters of different types of bursts. Three clusters were identified, with the frequency of each type peaking at a different part of the monsoon season. Further details may be found in Mohanty, Jakob, and Singh (2024).

Here, we are interested in applying a similar cluster analysis to that described above to model results. There are several ways to generate burst types from the models. One option is to perform an independent cluster analysis for each model. While technically straightforward and intuitively attractive, this approach has been shown to make multi-model comparisons to observations very difficult. This is because each model will produce its own independent set of clusters, making cross-model comparison and comparison to the observations difficult (Not shown). An alternative is to project the model-simulated rainfall burst characteristics onto the clusters calculated from the observational reference data set. This yields consistent burst types across all models and is the approach preferred here.

Specifically, we use the centroids of the reanalysis-based clusters as reference vectors, following Mohanty, Jakob, and Singh (2024). Each reference vector represents a 30-dimensional space defined by the 15-day evolution (from -7 to $+7$ days) of $[\nabla \cdot \{h\vec{v}\}]$ and $[\nabla \cdot \{s\vec{v}\}]$, which was used to construct the clusters. For each burst identified in the models, we extract its corresponding 30-dimensional vector and assign it to the nearest reanalysis cluster based on the shortest Euclidean distance. This approach ensures consistent and uniform cluster assignments across models. All analyses use ERA5-based clusters as the reference.

The main result of this analysis is the frequency of occurrence of each burst type in each of the models, which is summarized in Figure 8. The diagram has two axes that represent the frequency of bursts as a percentage on the y-axis and the burst type on the x-axis. The types are labeled C1, C2, and C3. C1 represents the archetypal active monsoon bursts, which resemble oceanic convection with a clear growth and decay phase and occur most frequently during the peak monsoon season. C2 corresponds to pre- and late-post-monsoon bursts, which are generally weak, localized rainfall events tied to coastal convection and often associated with trade-wind flow during the monsoon's build-up or retreat. C3 denotes strong and long-lasting bursts, frequently occurring near or after the monsoon retreat, often linked to tropical cyclones; these share the growth phase of C1 but lack a decay phase, maintaining high rainfall for at least a week (see Mohanty, Jakob, and Singh (2024) for more details). The color of each symbol in the figure indicates the seasonal-mean monsoon precipitation for each model. The four models with lower precipitation values than the reanalysis are denoted by circles, while those with higher values are denoted by squares. The reanalysis values are shown by stars. Furthermore, the position of the symbol within each cluster reflects its frequency of occurrence.

Figure 8 allows an analysis of the model errors in the frequency of occurrence of burst types and their relationship to mean precipitation. We find that higher mean precipitation values in the models are generally associated with higher active monsoon burst (C1) frequency percentages. Specifically, the models CanESM5, BCC-CSM2-MR, IPSL-CM6A-LR, and CESM2, denoted by square symbols, showed higher rainfall values than the reanalysis and all of them have higher percentages of C1 burst frequency against the reanalysis data. Models that overestimate active monsoon-like bursts generally compensate with an underestimation of the pre- and post-monsoon type bursts (C2), which are more prevalent in models with lower mean rainfall. The frequency of occurrence errors of strong bursts (C3), on the other hand, show no clear relationship to mean rainfall. This could be due to the fact that the most powerful bursts are often associated with cyclones, and there is no direct relationship between cyclone frequency and monsoon intensity (Weng et al., 2022).

To assess model performance more quantitatively, we calculate the RMSE between the frequency of occurrence values obtained from the reanalysis and the individual models. The MPI-ESM-1-2-LR model has the lowest RMSE when compared to the ERA5 reanalysis, indicating a higher level of accuracy in capturing the observed patterns whereas the CESM2 deviates the most, indicating potential limitations in their representation of monsoon dynamics. All the results are summarized in the 8th column of Table 2.

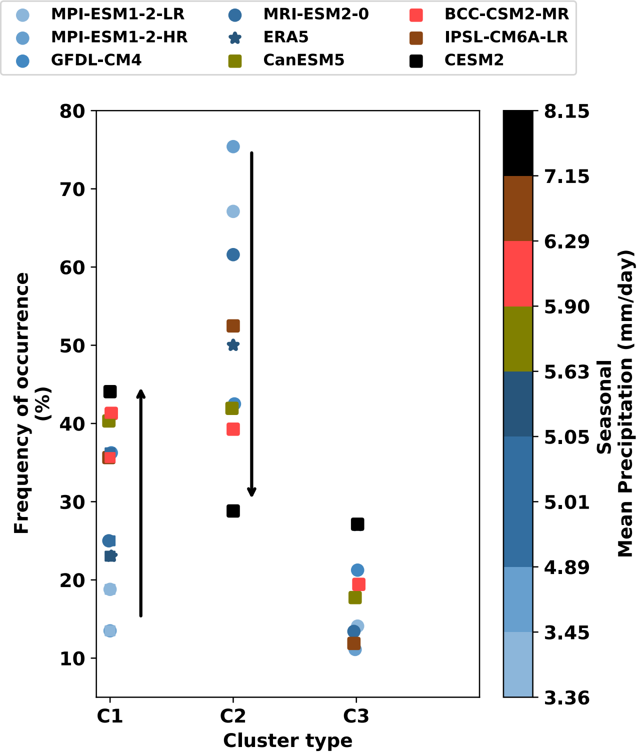

Figure 8. Frequency of occurrence of burst types using the ERA5 as a reference. See text for more details.

3.1.6. Overall Model Ranking

The above analyses reveal a significant variation in model performance across the different measures applied. To help further analysis we create a summary model ranking in the following way. We first rank each model individually for each result. Then, we compute the average rank for each model and rank the average values to find the final model ranking (as shown in the last column of Table 2). These comparisons show that MRI-ESM2-0 and GFDL-CM4 reproduce the gradual amplification and decay of bursts most consistently with reanalysis, while CESM2, BCC-CSM2-MR, and MPI-ESM-1-2-HR display deviations linked to differences in the representation of the evolution of dominant horizontal MSE and moisture advection.

Our original goal was to use this result to investigate potential relationships between model quality and model behavior in a future climate in the next section. Unfortunately, only three models (MRI-ESM2-0, IPSL-CM6A-LR, and BCC-CSM2-MR) provided the necessary AMIP+4K output for such an analysis. Importantly, our evaluation results show that these three models correspond to good, moderate, and relatively poor representations of MSE budget and rainfall bursts, respectively. The availability of these models therefore provides a resource to at least qualitatively study potential changes in burst characteristics under future climate conditions and how they might be related to model performance.

The burst-based ranking in this study differs from the precipitation-based ranking in Mohanty, Singh, and Jakob (2024). Although burst frequency and mean precipitation are positively correlated, they are not identical metrics. Bursts contribute between 40% (CanESM5) and 79% (MPI-ESM-1-2-LR) of total monsoon rainfall across the models, with the remainder coming from non-burst periods. As a result, a model may reproduce seasonal mean precipitation reasonably well but still misrepresent burst frequency or dynamics. Moreover, because our analysis combines the underlying physical mechanisms associated with the burst fraction of rainfall, the resulting ranking naturally differs from a precipitation-only assessment.

3.2. Model Behavior in an Idealized Warming Scenario

3.2.1. Precipitation in AMIP and AMIP+4K

The objective of this subsection is to explore the seasonal mean precipitation and the associated number of bursts within an idealized climate change scenario—AMIP+4K. We opted for the AMIP+4K future runs for our analysis as they simulate projected future climate conditions with increased radiative forcing, corresponding to a 4 Kelvin (K) global warming compared to pre-industrial levels. As discussed above, because of data availability, the following analyses can only be performed for three of the eight models used in the previous subsection. Of those, our model evaluation performed above has revealed the MRI-ESM2-0 model is regarded as the best, the IPSL-CM6A-LR model as intermediate, and the BCC-CSM2-MR model as the worst of the three models in regards to reproducing the MSE budget of monsoon bursts found in reanalysis.

It should be noted, however, that the AMIP+4K framework does not capture the patterned SST responses typically simulated by coupled models, which often exhibit an El Niño–like warming pattern rather than a spatially uniform increase (Cai et al., 2015). These non-uniform SST variations significantly impact regional monsoon climate by altering mean precipitation, atmospheric circulation, and horizontal moisture gradients, thus influencing the MSE budget. Consequently, the results presented here should be interpreted as idealized responses to a uniform warming scenario, while the role of patterned SST changes warrants further investigation using coupled model experiments or patterned-SST perturbation frameworks.

We begin our analysis by assessing changes in mean seasonal precipitation and burst characteristics under warming. For the MRI-ESM2-0 model, the AMIP+4K precipitation increases marginally to 5.04 mm/day compared to 5 mm/day in AMIP simulations. However, the number of burst events decreases slightly, from 164 in AMIP to 143 in AMIP+4K. A similar behavior is observed in the BCC-CSM2-MR model, which is generally regarded as the least skillful in simulating the current climate. Here, the mean precipitation remains unchanged at 5.9 mm/day across both simulations, with only a slight reduction in burst frequency from 247 to 245. In contrast, the IPSL-CM6A-LR model shows a substantial increase in mean precipitation from 6.3 mm/day in AMIP to 7.2 mm/day in AMIP+4K. Interestingly, despite this increase, the number of bursts declines markedly from 202 to 146. All the results are summarized in Table 3.

To explore these changes further, we examine the composite temporal evolution of precipitation during bursts in both AMIP and AMIP+4K simulations (Figure 9). Bursts in each simulation are identified using their respective seasonal climatology to ensure internal consistency. The blue and red lines in Figure 9 represent the composite burst precipitation for AMIP and AMIP+4K simulations, respectively, with the shaded regions indicating their standard deviations. MRI-ESM2-0 and IPSL-CM6A-LR models (Figures 9a and 9b) show similar precipitation evolution patterns across the two simulations—gradual intensification from day −7 to day +1, peaking at the same time, followed by a gradual decline. However, subtle differences emerge: MRI-ESM2-0 shows slightly higher peak precipitation in AMIP, while IPSL-CM6A-LR exhibits a pronounced increase in AMIP+4K. This suggests that IPSL-CM6A-LR simulates more intense bursts under warming, whereas MRI-ESM2-0 suggests a weakening of burst intensity. In contrast, BCC-CSM2-MR (Figure 9c) displays a less gradual burst evolution, with precipitation rising abruptly from day −2 and peaking on day 0. This abruptness, along with minimal changes in burst statistics, suggests that BCC-CSM2-MR fails to accurately capture the dynamical evolution of burst events, despite simulating similar mean precipitation and burst counts as MRI-ESM2-0.

A more detailed breakdown reveals model-specific responses to warming. For MRI-ESM2-0, both the number and duration of bursts decrease, while intensity increases slightly (from 7.5 to 7.6 mm/day). Consequently, the contribution of bursts to total rainfall drops from 50.9% to 44%, suggesting an overall weakening of burst activity. In the IPSL-CM6A-LR model, although the number of bursts declines, both duration (from 11.5 to 13.9 days) and intensity (from 8.6 to 8.9 mm/day) increase. This indicates more persistent and slightly stronger events; yet, their contribution to total rainfall declines from 50.5% to 40.2%, implying increased precipitation outside burst periods. The BCC-CSM2-MR model, on the other hand, shows negligible change in burst frequency and duration, with a slight reduction in intensity (from 13.9 to 13.5 mm/day) and a marginal decrease in burst contribution from 63.2% to 62.4%, highlighting its relative insensitivity to warming. A summary of all results is provided in the fifth, sixth, and seventh columns of Table 3.

While the number of burst events decreases across all models under warming, mean seasonal precipitation remains stable or even increases. This apparent contradiction arises from the burst definition, which depends on

Table 3

Summary of Burst Characteristics and Seasonal Mean Precipitation for Each Model Under AMIP and AMIP+4K Experiments

Model	Experiment	Mean precipitation (mm/day)	Total bursts	Average burst duration (Days)	Average day 0 precipitation (mm/day)	% of total precipitation	Bursts (C1)	Bursts (C2)	Bursts (C3)
MRI-ESM2-0	AMIP	5.0	164	13	7.5	50.9	41	101	22
	AMIP+4K	5.0	143	11.8	7.6	44	22	100	21
IPSL-CM6A-LR	AMIP	6.3	202	11.5	8.6	50.5	72	106	24
	AMIP+4K	7.2	146	13.9	8.9	40.2	59	64	23
BCC-CSM2-MR	AMIP	5.9	247	9.3	13.9	63.2	102	97	48
	AMIP+4K	5.9	245	9.4	13.5	62.4	83	105	49

Note. Reported values include mean precipitation, total number of bursts, average burst duration, average precipitation on the burst onset day (day 0), the percentage of total precipitation contributed by bursts, and the distribution of bursts across clusters C1, C2, and C3.

sharp transitions between dry and wet states. In warmer simulations, rainfall often intensifies more gradually or fluctuates around threshold values, leading to fewer events being classified as bursts. Model-specific responses also emerge: IPSL-CM6A-LR shows bursts becoming longer and slightly more intense, MRI-ESM2-0 suggests a weakening of burst structure, and BCC-CSM2-MR remains largely unchanged. Despite these differences, a growing share of rainfall occurs outside traditionally defined burst periods. Notably, the reduction in burst precipitation is observed across models with varying mean rainfall responses, pointing to a potentially robust signal. This may indicate a structural change in the Australian monsoon under warming, where precipitation becomes less bursty and more evenly distributed throughout the season. However, further analysis is needed to disentangle this physical shift from potential limitations in the burst detection methodology. Together, these findings underscore the need for adaptive metrics and a deeper understanding of model behavior to accurately capture evolving sub-seasonal precipitation patterns in a warming climate.

Similar to the AMIP evaluation, Figure 10 reproduces the approximate MSE-budget diagnostics (Equation 8) for the three models examined in the warming experiments, showing AMIP on the left column (panels a, c, e) and AMIP+4 K on the right column (panels b, d, f). The plotted terms are the MSE divergence $[\nabla \cdot \{h\mathbf{v}_h\}]$ (red, dashed), the linear NEF fit $\gamma[\nabla \cdot \{s\mathbf{v}_h\}] + \beta$ (black, dashed), their difference $(\gamma[\nabla \cdot \{s\mathbf{v}_h\}] + \beta) - ([\nabla \cdot \{h\mathbf{v}_h\}])$ (thick blue), and the storage term $\partial_t\{L_v q\}$ (olive, dashed). As established in the MSE framework, a physically consistent budget requires the storage term and the difference term to coincide, since both together represent the right-hand side of Equation 8. Their agreement therefore provides a direct measure of how well the model maintains energetic closure under warming already discussed in previous section. Similar to AMIP (Figure 3), the MSE divergence remains the primary driver of the budget evolution, and the NEF fit acts as a slowly varying background offset.

In MRI-ESM2-0 (panels a–b), the storage and difference terms remain tightly aligned throughout the burst cycle, even under the +4K perturbation. The amplification and decay phases broaden slightly but preserve their smooth

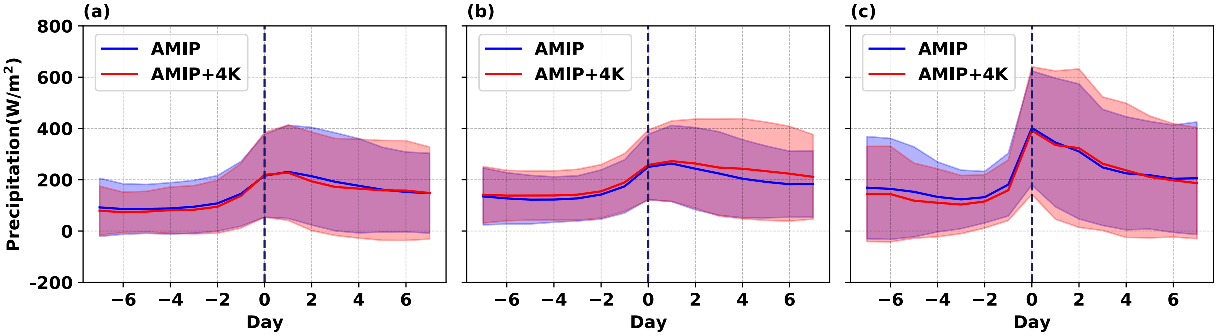

Figure 9. Burst composite temporal evolution of precipitation for AMIP (thick blue) and AMIP+4K simulations for (a) MRI-ESM2-0, (b) IPSL-CM6A-LR, and (c) BCC-CSM2-MR. The shaded area represents the standard deviation.

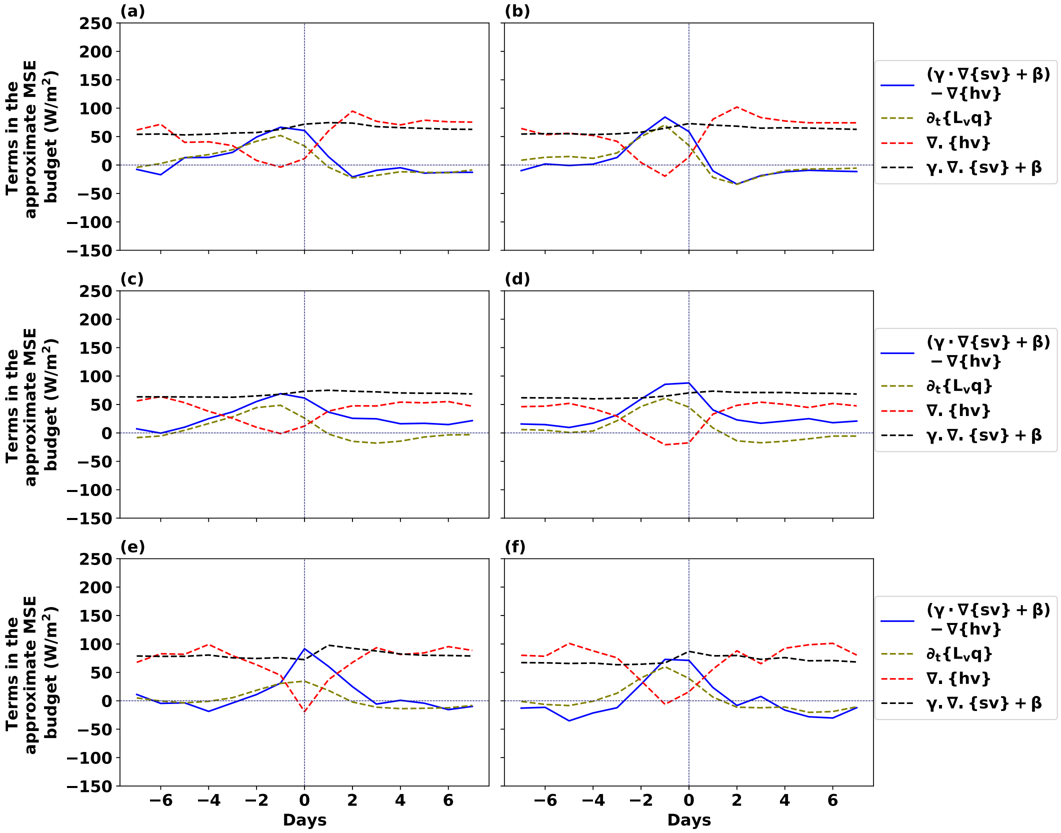

Figure 10. Terms in the approximate MSE budget (Equation 8) for both AMIP and AMIP+4K simulations in which $(\gamma[\nabla \cdot \{s\vec{v}\}] + \beta) - [\nabla \cdot \{h\vec{v}\}]$, storage, $[\nabla \cdot \{h\vec{v}\}]$, and $\gamma[\nabla \cdot \{s\vec{v}\}] + \beta$—are indicated by thick blue, dashed olive, dashed red, and dashed black lines, respectively. Panels (a) and (b) correspond to MRI-ESM2-0 AMIP and AMIP+4K, panels (c) and (d) to IPSL-CM6A-LR AMIP and AMIP+4K, and panels (e) and (f) to BCC-CSM2-MR AMIP and AMIP+4K.

temporal evolution, indicating that MRI-ESM2-0 sustains its physically realistic coupling between MSE divergence and moisture storage. This close correspondence confirms MRI-ESM2-0's robustness in replicating the burst energetics under warming.

IPSL-CM6A-LR (panels c–d) continues to show a gradual temporal evolution similar to its AMIP counterpart, but a consistent gap remains between the storage and difference traces. Although the overall shape of the curves is comparable, this persistent separation implies that IPSL-CM6A-LR does not fully capture the energetic balance linking large-scale advection to local storage, even when warmed. The model thus reproduces the general timing of bursts but not the complete physical mechanism behind their amplification and decay.

In BCC-CSM2-MR (panels e–f), the burst life cycle remains abrupt and strongly peaked, with both amplification and decay occurring over a short period. The separation between the storage and difference terms increases relative to MRI-ESM2-0 and IPSL-CM6A-LR, indicating the weakest budget closure. This behavior suggests that, even under warming, BCC-CSM2-MR fails to represent the MSE-driven balance that governs burst evolution, leading to unrealistic energetic variability.

Across all three models, the +4K warming modifies amplitudes only modestly and leaves the timing and phasing largely unchanged. The essential MSE-driven structure of the bursts therefore persists, but the quality of the physical closure differs sharply among models: MRI-ESM2-0 maintains excellent agreement between storage and difference, IPSL-CM6A-LR shows an unclosed energy budget, and BCC-CSM2-MR continues to deviate strongly. In summary, both AMIP and AMIP+4K simulations exhibit similar amplification and decay phases, as also reflected in the precipitation composites, with the main difference arising from precipitation magnitude rather than from changes in dynamical structure or MSE balance.

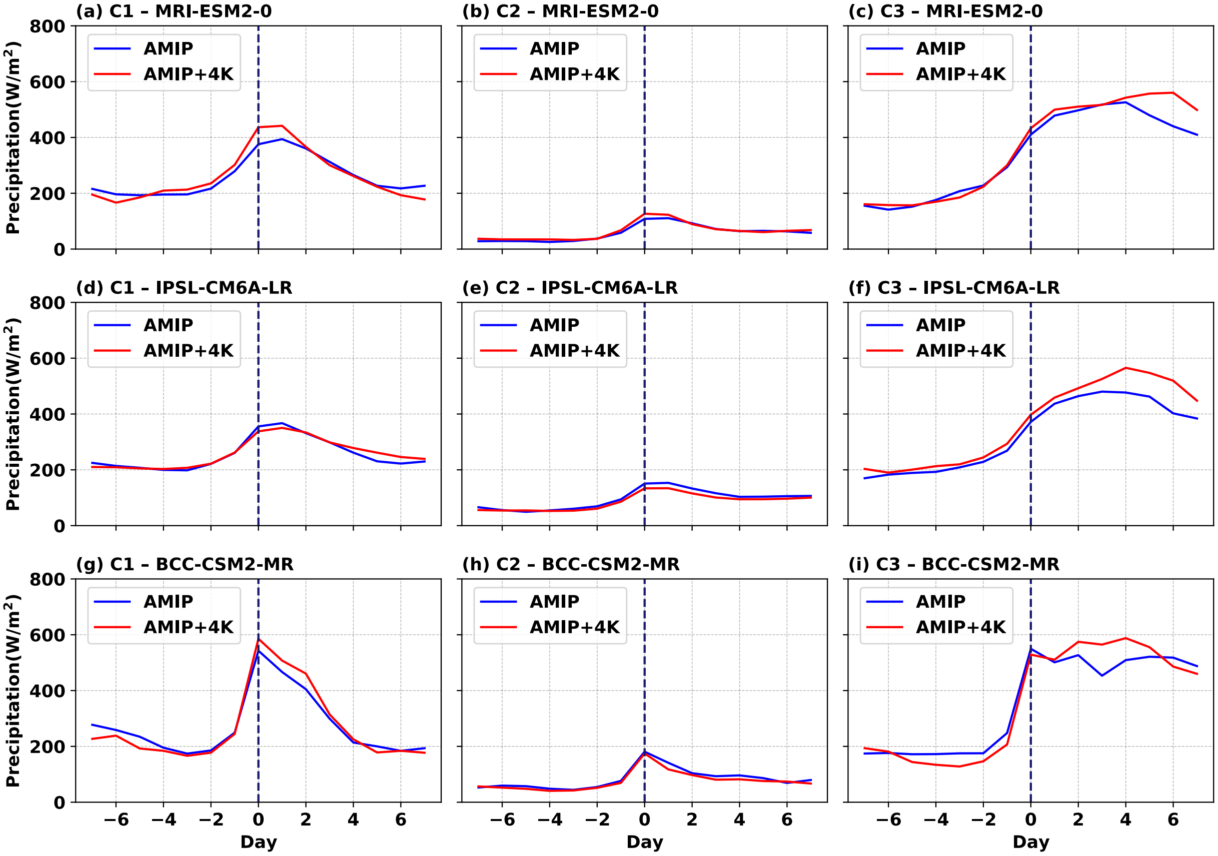

Figure 11. Comparisons of the temporal evolution of precipitation between the AMIP (thick blue) and AMIP+4K (thick orange) simulations for three different climate models: Panels (a) C1, (b) C2, and (c) C3 in the MRI-ESM2-0 model. Panels (d–f) show the corresponding IPSL-CM6A-LR model results, while panels (g–i) show the BCC-CSM2-MR model results.

To explore variations across bursts, we analyze the three burst clusters defined in the previous section: C1 (active monsoon), C2 (pre- and late-post-monsoon bursts), and C3 (strong bursts), defined using the minimum Euclidean distance from ERA5 reference clusters. Figure 11 compares AMIP and AMIP+4K precipitation evolution for each cluster.

- *MRI-ESM2-0*: C1 bursts in AMIP+4K show higher precipitation magnitude but lower frequency (Table 3, Figure 11a). C2 and C3 have similar temporal evolution and frequency, with AMIP+4K showing slightly higher precipitation near day 0 (C2) (Table 3, Figure 11b) and during the decay phase (C3) (Table 3, Figure 11c).
- *IPSL-CM6A-LR*: C1 bursts have similar amplification but higher AMIP precipitation before and after day 0, with fewer bursts in AMIP+4K (Table 3, Figure 11d). C2 shows higher AMIP precipitation and frequency (Table 3, Figure 11e). C3 has higher AMIP+4K precipitation but similar frequency (Table 3, Figure 11f).
- *BCC-CSM2-MR*: C1 has higher AMIP+4K precipitation but fewer bursts (Table 3, Figure 11g). C2 shows higher AMIP precipitation but fewer bursts (97 vs. 105) (Table 3, Figure 11h). C3 has similar burst counts, with AMIP higher during amplification and AMIP+4K higher during decay (Table 3, Figure 11i).

Our analysis highlights distinct model responses to idealized warming. MRI-ESM2-0, the best-performing model, preserves a consistent link between seasonal precipitation and burst frequency, with a slight decline in bursts. IPSL-CM6A-LR shows increased mean precipitation but a sharp drop in burst counts, breaking the earlier relationship. BCC-CSM2-MR continues to show abrupt, unrealistic precipitation changes with minimal variation in burst or mean precipitation. Cluster-wise analysis shows that MRI-ESM2-0 and IPSL-CM6A-LR both maintain physically consistent burst amplification and decay, though with different sensitivities to warming. In contrast, BCC-CSM2-MR exhibits abrupt transitions across all clusters, suggesting shortcomings in its representation of the mechanisms controlling burst evolution.

Figures 9 and 11 reveal that precipitation bursts in the AMIP and AMIP+4K scenarios share a qualitatively similar temporal evolution, with consistent amplification and decay phases, though the precipitation magnitude varies notably across models and burst types, suggesting that warming primarily alters precipitation intensity without altering the core burst life cycle. To understand these intensity differences, we turn to the moisture budget for a clearer diagnostic perspective. In contrast to Section 3.1, which employed the MSE budget and moisture tendency term ($\partial_t[L_v q]$) to analyze the burst life cycle in the present climate by tracking amplification and decay, Section 3.2.2 focuses on comparing precipitation responses between the AMIP and AMIP+4K scenarios. Here, the moisture budget directly links precipitation changes to variations in evaporation and moisture advection, which will be examined in detail in the following subsection.

3.2.2. Moisture Budget Analysis of Precipitation Change

The moisture budget, analogous to the MSE budget outlined in the methodology section, can be expressed as:

$$-\partial_t\{L_v q\} - \nabla\cdot\{L_v q\vec{v}_h\} + L_v E = L_v P, \tag{10}$$

where $\partial_t\{L_v q\}$ represents the moisture tendency, and $\nabla\cdot\{L_v q\vec{v}_h\}$ denotes the moisture divergence. Neglecting second-order terms, the precipitation differences between the two simulations can be written on the basis of the moisture budget as:

$$\Delta[(LP)] = \Delta[(L_v E)] + \Delta(-[(\nabla\cdot\{L_v q\vec{v}\})]) + \Delta(-[(\partial_t\{L_v q\})]), \tag{11}$$

Similar to Equation 9, the term $\Delta(-[(\nabla\cdot\{L_v q\vec{v}\})]$ can be decomposed into its vertical and horizontal advection components. Accordingly, Equation 11 can be written as:

$$\Delta[(LP)] = \Delta[(L_v E)] + \Delta(-[(\{\omega\partial_p L_v q\})]) + \Delta(-[(\{\vec{v}\cdot\nabla L_v q\})]) + \Delta(-[(\partial_t\{L_v q\})]), \tag{12}$$

where Δ is the difference between AMIP+4K and AMIP. $\Delta(-[(\nabla\cdot\{L_v q\vec{v}\})])$ is the difference in moisture flux convergence in the energy unit, which has two components: the difference in vertical advection ($\Delta[(-(\{\omega\partial_p L_v q\})])$) and horizontal advection ($\Delta(-[(\{\vec{v}\cdot\nabla L_v q\})])$) (Equation 12). Positive (negative) values of the above two components contribute to an increase (decrease) in precipitation in AMIP+4K compared to AMIP. $\Delta(-[(\partial_t\{L_v q\})])$ and $\Delta[(L_v E)]$ represent the difference in the storage term and evaporation, respectively. Overall, by comparing the components from the right-hand side of Equation 12 with the precipitation change, we can gain a better understanding of the factors affecting the precipitation change. While our analysis can provide useful insights, we recognize the limitations of conserved variable budget analyses in identifying cause and effect in physical relationships. Doing so will require more directed process studies that are left to future work. From this section onwards, we have only considered the MRI-ESM2-0 and IPSL-CM6A-LR as for BCC-CSM2-MR, the daily vertical velocity field is not available. Figure 12 summarizes the terms of Equation 12. Thick blue, thick red, dashed green, dashed purple, and dashed olive lines indicate differences in precipitation, vertical advection, horizontal advection, storage tendency, and evaporation.

Figure 12 depicts two key findings from the analysis of the MRI-ESM2-0 and IPSL-CM6A-LR models. There is a consistent relationship between changes in precipitation and vertical advection across all three clusters (thick blue vs. thick red lines). They have a strong correlation, indicating a strong relationship between these two terms. Second, changes in the storage tendency and horizontal moisture advection have a reciprocal relationship, effectively canceling each other out. As a result, these terms either contribute minimally to precipitation changes or result in a constant temporal pattern (Figure 12) that primarily affects the magnitude of the variation without significantly influencing its overall temporal evolution. The change in evaporation remains approximately zero overall, contributing little to the changes in precipitation. As a result, the change in vertical advection appears to be the primary driver of the precipitation difference, emphasizing its critical role in shaping the variations in precipitation patterns.

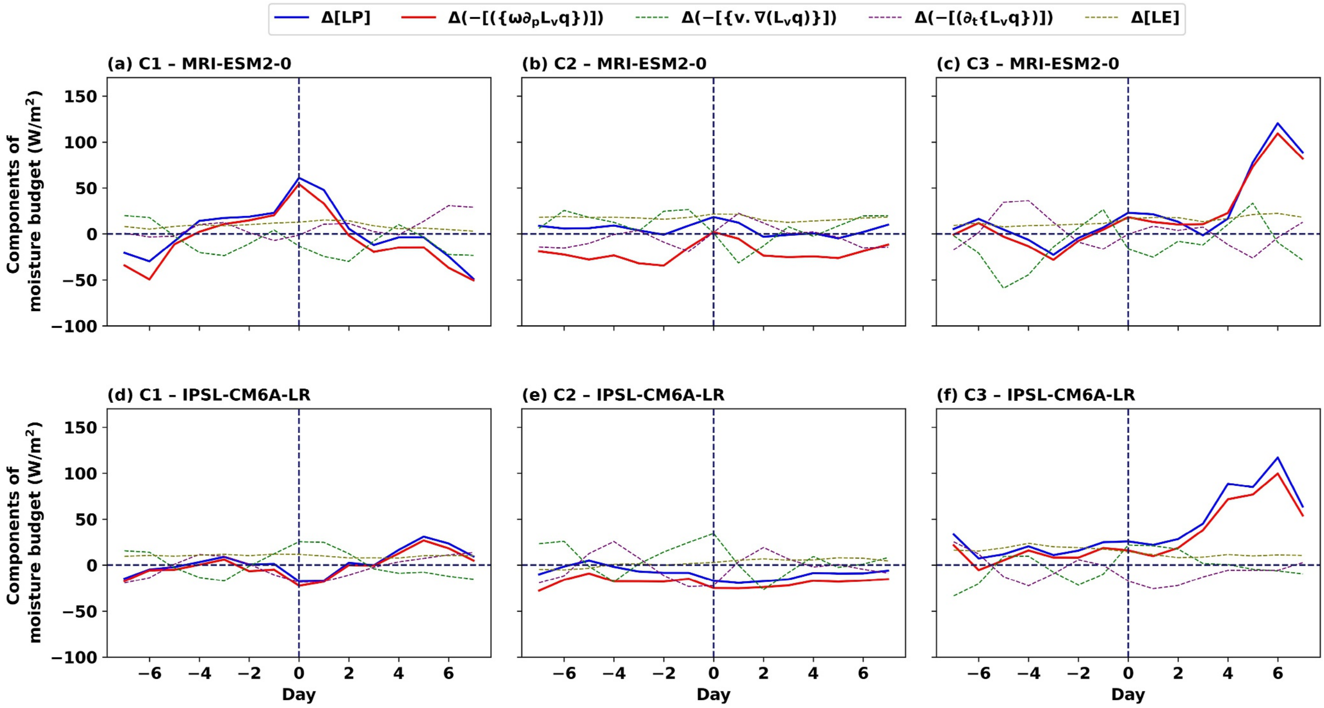

Figure 12. The temporal evolution of the precipitation difference between the AMIP+4K and AMIP simulations, as well as the causative components derived from the moisture budget analysis, for two different climate models. The MRI-ESM2-0 model results for C1, C2, and C3 are shown in panels (a)–(c), respectively. The IPSL-CM6A-LR model results are shown in panels (d)–(f).

3.2.3. Understanding the Dynamic and Thermodynamic Contribution of Vertical Advection Difference

As discussed in the previous section, changes in vertical advection of moisture appear to play a critical role in influencing precipitation differences between the AMIP and AMIP+4K simulations. To delve deeper into this result, further analysis will involve separating vertical advection into two distinct components: dynamic and thermodynamic (Seager & Vecchi, 2010; Seager et al., 2010). This decomposition will allow us to gain a more comprehensive understanding of these components' individual contributions to their overall changes. For this analysis, we divide the changes in vertical moisture advection into changes in vertical motion and changes in moisture. Once again, neglecting second-order terms this can be written as:

$$-\Delta[\{\omega\partial_p(L_v q)\}] \approx -\left[\left\{(\Delta\omega)\partial_p\left(L_v q_{\text{AMIP}}\right)\right\}\right] - [\{\omega_{\text{AMIP}}(\Delta\partial_p(L_v q))\}], \tag{13}$$

The dynamic and thermodynamic components are denoted by $-\left[\left\{(\Delta\omega)\partial_p\left(L_v q_{\text{AMIP}}\right)\right\}\right]$ and $-[\{\omega_{\text{AMIP}}(\Delta\partial_p(L_v q))\}]$. The terms of Equation 13 are combined in Figure 13 to determine how each component influences the overall variation in vertical advection. The difference in vertical advection along with its dynamic and thermodynamic components are marked with thick red, dashed blue, and dashed olive lines respectively. To provide additional insight, we also investigate the vertical profiles of $[\omega]$ and $[\partial_p L_v q]$ for burst day 0 for the two simulations (Figure 14; AMIP (dashed blue), AMIP+4K (dashed red)), averaged over the monsoon region. We find that overall both dynamic and thermodynamic influences are important in shaping the overall variation in the vertical advection component with some key differences between the two models.

In burst type C1 of MRI-ESM2-0, the vertical moisture advection difference in AMIP+4K is primarily driven by changes in both the dynamic and thermodynamic components (Figure 13a). Apart from around day 0, it remains negative throughout. The thermodynamic component is consistently positive, contributing to atmospheric moistening and leading to an increase in precipitation, whereas the dynamic component stays negative, resulting in drying. Around day 0, the positive magnitude of the thermodynamic component exceeds the negative contribution from the dynamic component, resulting in stronger net moistening and, consequently, higher precipitation in AMIP+4K (see the blue vs. red line in Figure 12a). The vertical distribution of $[\omega]$ and $[\partial_p L_v q]$ help

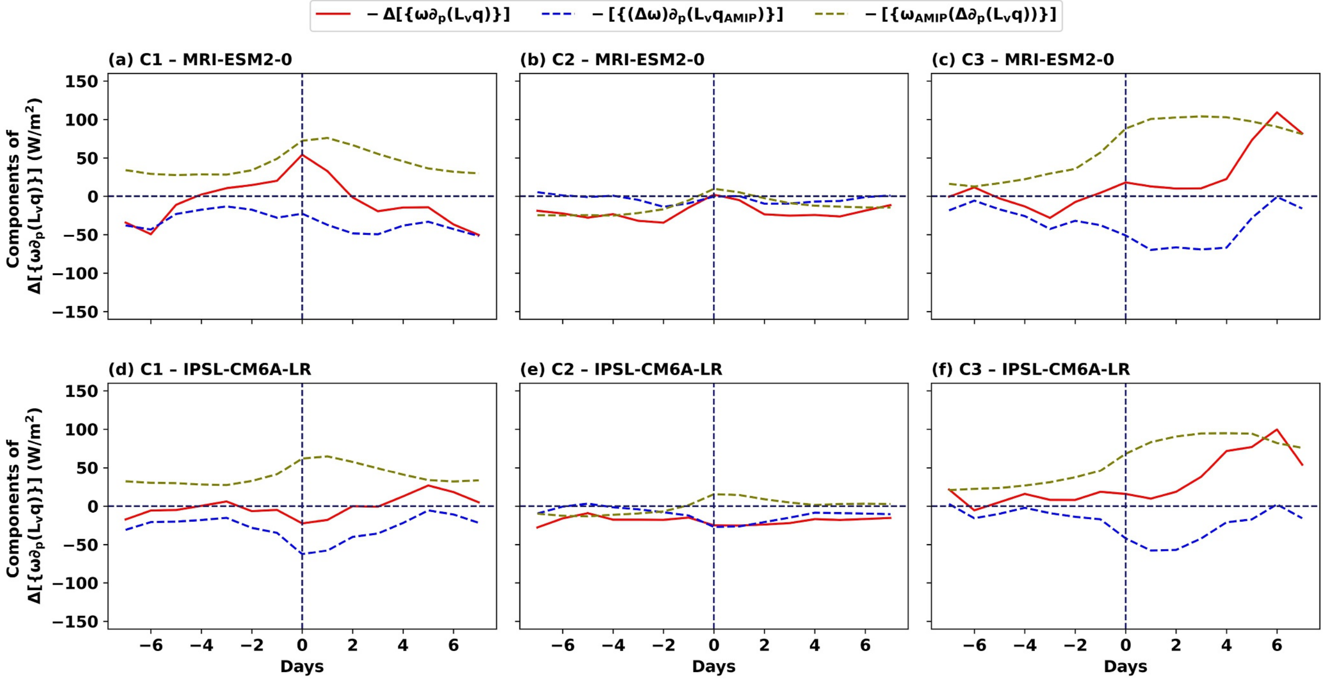

Figure 13. The temporal evolution of the vertical advection of moisture difference between the AMIP+4K and AMIP simulations, along with its dynamic and thermodynamic components, for two different climate models. Panels (a)–(c) depict the MRI-ESM2-0 model results for C1, C2, and C3, respectively. Panels (d)–(f) display the corresponding IPSL-CM6A-LR model results.

to better understand this relationship (Figure 14a). We see an increase in $[\partial_p L_v q]$, brought about by the warming in the model and the well-known Clausius-Clapeyron relationship. Concurrently, there is a weakening of $[\omega]$ on day 0 in the AMIP+4K simulation. Combining the weaker $[\omega]$ with the positive difference of $[\partial_p L_v q]$, leads to the overall increase in the vertical advection term seen in Figure 13a. In summary, for the MRI-ESM2-0 model the significant increase in vertical advection of moisture can be primarily attributed to the thermodynamic component over the dynamic component.

For the C1 cluster in IPSL-CM6A-LR, on the other hand, the drying effect from the dynamical component tends to outweigh the moistening from the thermodynamic component, particularly around day 0. This leads to an overall reduction in vertical moisture advection in AMIP+4K compared to AMIP (Figure 13d). The vertical profile on day 0 confirms the above observation. Unlike MRI-ESM2-0, the weakening in $[\omega]$ is more pronounced in IPSL-CM6A-LR, while the $[\partial_p L_v q]$ difference maintains a similar magnitude to that in MRI-ESM2-0 throughout the column (Figure 14d). The pronounced weakening of $[\omega]$ enhances drying through the dynamic component, leading to a negative difference in vertical moisture advection. In summary, unlike in the MRI-ESM2-0 model, the moistening of the atmosphere by the thermodynamic component in the IPSL-CM6A-LR model is weaker than the drying caused by the dynamic component, resulting in an overall negative change in precipitation in AMIP+4K compared to AMIP (Figure 11) on day 0.

In burst type C3, MRI-ESM2-0's vertical moisture advection difference is mostly positive, driven by the thermodynamic component in magnitude and both dynamic and thermodynamic components in temporal evolution, except briefly during amplification. In IPSL-CM6A-LR, it remains consistently positive, with both components influencing magnitude and evolution (Figure 13c vs Figure 13f). Similar to C1, MRI-ESM2-0's vertical profile on day 0 reinforces this pattern, showing a stronger positive thermodynamic contribution due to a larger positive difference in $[\partial_p L_v q]$ throughout the column. Meanwhile, the negative dynamic contribution is weaker, resulting from a modest decrease in $[\omega]$ in the upper and lower troposphere. Although differences in $[\omega]$ are more pronounced in the mid-troposphere, the integrated dynamic contribution remains smaller than the thermodynamic one (Figure 14c). Similarly, IPSL-CM6A-LR exhibits a comparable vertical profile of $[\omega]$ and $[\partial_p L_v q]$ on day 0, consistent with the observed changes in the vertical moisture advection difference (Figure 14f).

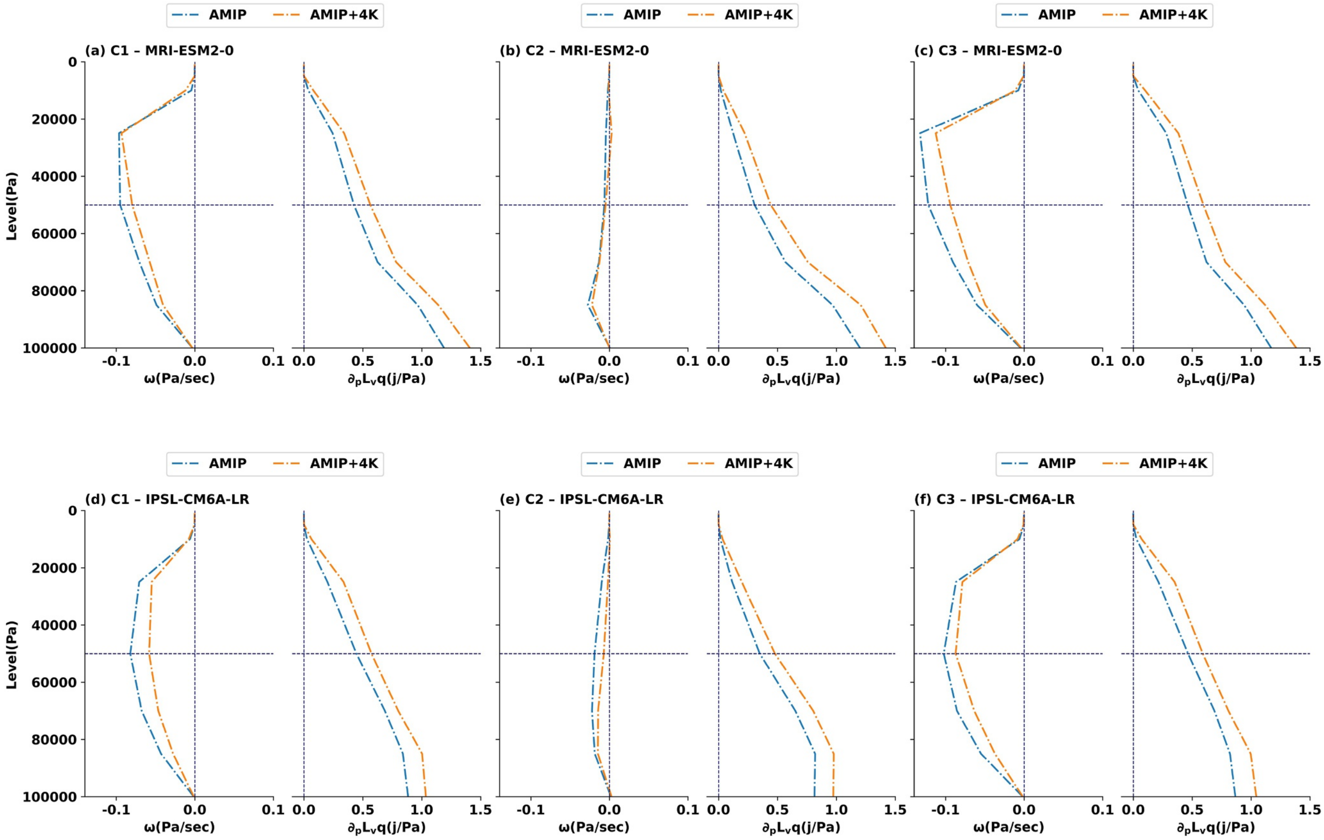

Figure 14. $[\omega]$ and $[\partial_p L_v q]$ comparisons for two different climate models on day 0 for the AMIP (dashed blue) and AMIP+4K (dashed red) simulations. The results of the MRI-ESM2-0 model for C1, C2, and C3 are shown in panels (a)–(c), respectively. The results of the corresponding IPSL-CM6A-LR model are shown in panels (d)–(f).

In burst type C2, changes in both models are always negative except for MRI-ESM2-0 during day 0. As with the other cluster types, both the dynamic and thermodynamic components contribute to the magnitude and temporal evolution. Notably, unlike C1 and C3, the thermodynamic component in C2 remains predominantly negative on most days, leading to drying rather than the moistening seen in the other two clusters, while the dynamic component is generally weak—either near zero or negative (dashed olive and blue lines in Figures 13b and 13e). In MRI-ESM2-0, the positive difference in $[\partial_p L_v q]$, combined with a weak $[\omega]$ profile in the AMIP simulation, leads to a modest positive thermodynamic contribution and an overall near-zero net effect from both the dynamic components on day 0 (Figure 14b). Additionally, days with negative thermodynamic components are associated with either a downward $[\omega]$ or a combination of upward and downward $[\omega]$ across pressure levels, resulting in an overall negative column integration, given that $[\partial_p L_v q]$ remains positive due to the Clausius-Clapeyron relation. However, in IPSL-CM6A-LR, a relatively larger decrease in $[\omega]$ leads to a more negative dynamic component, resulting in an overall negative vertical moisture advection difference, in contrast to the negligible change observed in MRI-ESM2-0 (Figure 14e).

Overall, the MRI-ESM2-0 and IPSL-CM6A-LR models exhibit distinct behaviors in how dynamic and thermodynamic components influence vertical moisture advection, particularly on day 0. In the MRI-ESM2-0 model, increased moisture advection—and thus higher precipitation in bursts C1 and C3—is primarily driven by the thermodynamic component. Conversely, in the IPSL-CM6A-LR model, the dynamic component plays a stronger role; notably in burst C1, a pronounced weakening of vertical motion leads to drying that outweighs the thermodynamic moistening. This dynamic dominance also contributes to reduced precipitation in burst C2. Overall, the MRI-ESM2-0 model responds to warming with increased precipitation, while the IPSL-CM6A-LR model shows a more mixed, often negative response, underscoring model-specific differences in vertical moisture advection processes.

4. Summary and Conclusion

The primary goal of this paper was to examine into the dynamics underlying the evolution of Australian monsoon bursts in climate models, evaluate their ability to replicate results from a reanalysis and assess how they change under an idealized warming scenarios. To accomplish this, we used AMIP simulations of eight CMIP6 models and compared the statistics and dynamics to ERA5. In addition, we have expanded our analysis to include AMIP+4K simulations from three CMIP6 models to investigate their behavior under warming conditions. Our investigation has yielded the following key findings:

- Previous research has found that models with a high seasonal mean precipitation tend to produce more bursts than models with a low seasonal mean precipitation (Narsey et al., 2018). Our analysis confirms this finding for AMIP simulations and further shows a strong relationship between seasonal mean precipitation and burst type. Specifically, CMIP6 models with higher seasonal mean precipitation exhibit a greater proportion of active monsoon bursts (C1), which resemble oceanic convection with clear growth and decay phases during the peak monsoon season. In contrast, models with lower seasonal mean precipitation have a relatively higher proportion of pre- and late-post-monsoon bursts (C2), which are weaker, localized events tied to coastal convection. This interpretation is consistent with the burst-type framework of Mohanty, Jakob, and Singh (2024), where C1 bursts are associated with oceanic convection and C2 bursts with coastal convection. Thus, the differences across models can be understood as reflecting how their mean state precipitation modulates the balance between oceanic (C1) and coastal (C2) convective regimes, with low-precipitation models favoring the latter.
- The composite of monsoon bursts in AMIP simulations exhibits many similarities to ERA5. In almost all models, the evolution of MSE divergence is dominated by horizontal moisture advection, with the exception of BCC-CSM2-MR and CESM2, which are dominated by vertical MSE advection along with horizontal advection. The inclusion of an analysis of the GMS-based drying efficiency highlighted the pronounced growth phase of convection before the burst peak and a weaker decay phase after the peak in most models, with the exception of IPSL-CM6A-LR, which underrepresented the decay phase due to an imbalance between the drying efficiency term and the moisture tendency. In the context of the composite and the separation of bursts into clusters, MRI-ESM2-0 emerges as one of the more accurate models in replicating the dynamics seen in the reanalysis, while BCC-CSM2-MR, CESM2, and MPI-ESM-1-2-HR significantly deviate from the reanalysis. The notable disparities among the models can likely be attributed to differences in their parameterization schemes, but further research is needed to confirm this.
- When comparing bursts between the AMIP and AMIP+4K simulations, MRI-ESM2-0 and BCC-CSM2-MR reproduce seasonal precipitation patterns similar to their AMIP counterparts, with burst frequencies remaining consistent in BCC-CSM2-MR and slightly reduced in MRI-ESM2-0. However, only MRI-ESM2-0 captures a gradual burst evolution, resembling both the reanalysis and its AMIP simulation, whereas BCC-CSM2-MR continues to exhibit abrupt transitions similar to its AMIP version. IPSL-CM6A-LR, while also exhibiting gradual burst evolution like MRI-ESM2-0, displays a distinct response under warming—producing fewer but longer and more intense bursts, alongside a notable increase in mean precipitation. These differing model behaviors show that while some changes—like the overall drop in burst frequency—are fairly consistent across models, the details of how bursts form and behave vary a lot. MRI-ESM2-0's response appears more physically consistent, which gives us more confidence in its projections. In contrast, the variability seen in IPSL-CM6A-LR and the shortcomings in BCC-CSM2-MR underscore how crucial it is to carefully assess each model's individual behavior when trying to understand future changes in rainfall.
- When examining the composite of clusters, notable differences emerge across the three models under warming. For C1, MRI-ESM2-0 and BCC-CSM2-MR show an increase in precipitation, while IPSL-CM6A-LR exhibits either a decrease or no significant change. In C2, MRI-ESM2-0 again indicates an increase, whereas IPSL-CM6A-LR and BCC-CSM2-MR both show a decrease in the AMIP+4K simulations. In C3, all models consistently show increased precipitation under warming. A deeper analysis reveals that differences in composite precipitation arise from how dynamic and thermodynamic components influence vertical moisture advection. In MRI-ESM2-0, enhanced precipitation in bursts C1 and C3 is mainly driven by stronger thermodynamic moisture advection. In contrast, in IPSL-CM6A-LR, dynamic processes dominate; for instance, in burst C1, a weakening of vertical motion leads to drying that offsets thermodynamic moistening. This dynamic dominance in IPSL-CM6A-LR also contributes to reduced precipitation in burst C2. These results highlight model-specific behaviors in the interplay of dynamics and thermodynamics, emphasizing the complexity of

precipitation responses to warming in different climate models. In future research, exploring the interplay between thermodynamic and dynamic interactions, as discussed in the study by J. D. Neelin et al. (2022) could be a valuable addition.

In summary, this paper has provided insights into the relationships between seasonal mean precipitation, burst types, and model behavior, revealing significantly different behaviors among the available models and highlighting the existing uncertainties among climate models in both current and warming scenarios. Unfortunately, only a small subset of modeling groups have stored the necessary output to perform this analysis, which limits our conclusions on the relationship of model behavior in a warmer climate with its performance against reanalysis in the current climate.

Conflict of Interest

The authors declare no conflicts of interest relevant to this study.

Data Availability Statement

This study utilizes ERA5 reanalysis data as the primary atmospheric data set. The ERA5 system is described in Hersbach et al. (2020). Specifically, we use ERA5 hourly data on pressure levels and ERA5 hourly data on single levels, obtained from the Copernicus Climate Change Service Climate Data Store (Hersbach et al., 2023a, 2023b). For model evaluation, we use AMIP and AMIP+4K simulations from the CMIP6 archive (Eyring et al., 2016), accessed via the Earth System Grid Federation at https://esgf-ui.ceda.ac.uk/search. All figures presented in this manuscript were generated using Python.

Acknowledgments

This research was supported by the Australian Research Council (ARC) Centre of Excellence for Climate Extremes (CE170100023) and the ARC Discovery Project (DP200102954). M.S. acknowledges support from the Australian Government Research Training Program Scholarship. Computational resources were provided by the National Computational Infrastructure (NCI), supported by the Australian Government. Assistance from a large language model (ChatGPT, developed by OpenAI) was used to improve the clarity and grammar of the manuscript. Open access publishing facilitated by Monash University, as part of the Wiley - Monash University agreement via the Council of Australasian University Librarians.

References

Adames, Á. F., & Kim, D. (2016). The MJO as a dispersive, convectively coupled moisture wave: Theory and observations. *Journal of the Atmospheric Sciences*, *73*(3), 913–941. https://doi.org/10.1175/jas-d-15-0170.1

Allan, R. J. (1988). El Niño southern oscillation influences in the Australasian region. *Progress in Physical Geography*, *12*(3), 313–348. https://doi.org/10.1177/030913338801200301

Allen, M. R., & Ingram, W. J. (2002). Constraints on future changes in climate and the hydrologic cycle. *Nature*, *419*(6903), 224–232. https://doi.org/10.1038/nature01092

Berry, G. J., & Reeder, M. J. (2016). The dynamics of Australian monsoon bursts. *Journal of the Atmospheric Sciences*, *73*(1), 55–69. https://doi.org/10.1175/JAS-D-15-0071.1

Berry, G. J., Reeder, M. J., & Jakob, C. (2012). Coherent synoptic disturbances in the Australian monsoon. *Journal of Climate*, *25*(24), 8409–8421. https://doi.org/10.1175/JCLI-D-12-00143.1

Brown, J. R., Moise, A. F., Colman, R., & Zhang, H. (2016). Will a warmer world mean a wetter or drier Australian monsoon? *Journal of Climate*, *29*(12), 4577–4596. https://doi.org/10.1175/JCLI-D-15-0695.1

Bui, H. X., Yu, J.-Y., & Chou, C. (2016). Impacts of vertical structure of large-scale vertical motion in tropical climate: Moist static energy framework. *Journal of the Atmospheric Sciences*, *73*(11), 4427–4437. https://doi.org/10.1175/JAS-D-16-0031.1

Cai, W., Wang, G., Santoso, A., McPhaden, M. J., Wu, L., Jin, F.-F., et al. (2015). Increased frequency of extreme La Niña events under greenhouse warming. *Nature Climate Change*, *5*(2), 132–137. https://doi.org/10.1038/nclimate2492

Charney, J. G. (1969). A further note on large-scale motions in the tropics. *Journal of the Atmospheric Sciences*, *26*(1), 182–185. https://doi.org/10.1175/1520-0469(1969)026<0182:afnols>2.0.co;2

Chung, C., Boschat, G., Taschetto, A., Narsey, S., McGregor, S., Santoso, A., & Delage, F. (2023). Evaluation of seasonal teleconnections to remote drivers of Australian rainfall in CMIP5 and CMIP6 models. *Journal of Southern Hemisphere Earth Systems Science*, *73*(3), 219–261. https://doi.org/10.1071/es23002

Dong, T., & Dong, W. (2021). Evaluation of extreme precipitation over Asia in CMIP6 models. *Climate Dynamics*, *57*(7–8), 1751–1769. https://doi.org/10.1007/s00382-021-05773-1

Emori, S., & Brown, S. (2005). Dynamic and thermodynamic changes in mean and extreme precipitation under changed climate. *Geophysical Research Letters*, *32*(17), L17706. https://doi.org/10.1029/2005gl023272

Eyring, V., Bony, S., Meehl, G. A., Senior, C. A., Stevens, B., Stouffer, R. J., & Taylor, K. E. (2016). Overview of the coupled model intercomparison project phase 6 (CMIP6) experimental design and organization. *Geoscientific Model Development*, *9*(5), 1937–1958. https://doi.org/10.5194/gmd-9-1937-2016

Gadgil, S. (2018). The monsoon system: Land–sea breeze or the ITCZ? *Journal of Earth System Science*, *127*(1), 1–29. https://doi.org/10.1007/s12040-017-0916-x

Grose, M. R., Narsey, S., Delage, F., Dowdy, A. J., Bador, M., Boschat, G., et al. (2020). Insights from CMIP6 for Australia's future climate. *Earth's Future*, *8*(5), e2019EF001469. https://doi.org/10.1029/2019ef001469

Held, I. M., & Soden, B. J. (2006). Robust responses of the hydrological cycle to global warming. *Journal of Climate*, *19*(21), 5686–5699. https://doi.org/10.1175/jcli3990.1

Hersbach, H., Bell, B., Berrisford, P., Biavati, G., Horányi, A., Muñoz Sabater, J., et al. (2023a). ERA5 hourly data on single levels from 1940 to present [Dataset]. *10. Copernicus Climate Change Service (C3S) Climate Data Store (CDS)*. https://doi.org/10.24381/cds.adbb2d47

Hersbach, H., Bell, B., Berrisford, P., Biavati, G., Horányi, A., Muñoz Sabater, J., et al. (2023b). ERA5 hourly data on pressure levels from 1940 to present [Dataset]. *Copernicus Climate Change Service (C3S) Climate Data Store (CDS)*, *10*, 24381. https://doi.org/10.24381/cds.bd0915c6

Hersbach, H., Bell, B., Berrisford, P., Hirahara, S., Horányi, A., Muñoz-Sabater, J., et al. (2020). The ERA5 global reanalysis. *Quarterly Journal of the Royal Meteorological Society*, *146*(730), 1999–2049. https://doi.org/10.1002/qj.3803

Hill, S. A., Ming, Y., Held, I. M., & Zhao, M. (2017). A moist static energy budget–based analysis of the Sahel rainfall response to uniform oceanic warming. *Journal of Climate*, *30*(15), 5637–5660. https://doi.org/10.1175/JCLI-D-16-0785.1

Hill, S. A., Ming, Y., & Zhao, M. (2018). Robust responses of the Sahelian hydrological cycle to global warming. *Journal of Climate*, *31*(24), 9793–9814. https://doi.org/10.1175/JCLI-D-18-0238.1

Inoue, K., & Back, L. E. (2015). Gross moist stability assessment during toga coare: Various interpretations of gross moist stability. *Journal of the Atmospheric Sciences*, *72*(11), 4148–4166. https://doi.org/10.1175/JAS-D-15-0092.1

Inoue, K., Biasutti, M., & Fridlind, A. M. (2021). Evidence that horizontal moisture advection regulates the ubiquitous amplification of rainfall variability over tropical oceans. *Journal of the Atmospheric Sciences*, *78*(2), 529–547. https://doi.org/10.1175/jas-d-20-0201.1

Jiang, X., Adames, Á. F., Zhao, M., Waliser, D., & Maloney, E. (2018). A unified moisture mode framework for seasonality of the Madden–Julian oscillation. *Journal of Climate*, *31*(11), 4215–4224. https://doi.org/10.1175/jcli-d-17-0671.1

Kajikawa, Y., Wang, B., & Yang, J. (2010). A multi-time scale Australian monsoon index. *International Journal of Climatology*, *30*(8), 1114–1120. https://doi.org/10.1002/joc.1955

Kim, K.-Y., Kullgren, K., Lim, G.-H., Boo, K.-O., & Kim, B.-M. (2006). Physical mechanisms of the Australian summer monsoon: 2. Variability of strength and onset and termination times. *Journal of Geophysical Research*, *111*(D20), D20105. https://doi.org/10.1029/2005jd006808

Kullgren, K., & Kim, K.-Y. (2006). Physical mechanisms of the Australian summer monsoon: 1. Seasonal cycle. *Journal of Geophysical Research*, *111*(D20), D20104. https://doi.org/10.1029/2005JD006807

Lau, W. K., Waliser, D. E., Wheeler, M., & McBride, J. (2005). *Australian-Indonesian monsoon*. Springer.

Li, Y., Du, M., Feng, J., Xu, F., & Song, W. (2023). Relationships between the Hadley circulation and tropical sea surface temperature with different meridional structures simulated in CMIP6 models. *Frontiers in Marine Science*, *10*, 1145509. https://doi.org/10.3389/fmars.2023.1145509

Lough, J. (1993). Variations of some seasonal rainfall characteristics in Queensland, Australia: 1921–1987. *International Journal of Climatology*, *13*(4), 391–409. https://doi.org/10.1002/joc.3370130404

Maloney, E. D. (2009). The moist static energy budget of a composite tropical intraseasonal oscillation in a climate model. *Journal of Climate*, *22*(3), 711–729. https://doi.org/10.1175/2008JCLI2542.1

Mapes, B., & Houze, R. A., Jr. (1992). An integrated view of the 1987 Australian monsoon and its mesoscale convective systems. I: Horizontal structure. *Quarterly Journal of the Royal Meteorological Society*, *118*(507), 927–963. https://doi.org/10.1002/qj.49711850706

Mapes, B., & Houze, R. A., Jr. (1993). An integrated view of the 1987 Australin monsoon and its mesoscale convective systems. II: Vertical structure. *Quarterly Journal of the Royal Meteorological Society*, *119*(512), 733–754. https://doi.org/10.1002/qj.49711951207

Mohanty, S. (2024). *Australian summer monsoon rainfall: A moist static energy budget perspective* (PhD Thesis). Monash University. https://doi.org/10.26180/25602252.v1

Mohanty, S., Garg, N., Ramesh, N., & Prakash, M. (2025). Precipitation bursts in northern Australia with and without preceding heatwaves. *Weather and Climate Extremes*, *51*, 100845. https://doi.org/10.1016/j.wace.2025.100845

Mohanty, S., Jakob, C., & Singh, M. S. (2024). Australian summer monsoon bursts: A moist static energy budget perspective. *Journal of Geophysical Research: Atmospheres*, *129*(1), e2023JD039048. https://doi.org/10.1029/2023jd039048

Mohanty, S., Singh, M. S., & Jakob, C. (2024). Australian summer monsoon: Reanalyses versus climate models in moist static energy budget evolution. *Journal of Geophysical Research: Atmospheres*, *129*(12), e2023JD040162. https://doi.org/10.1029/2023jd040162

Narsey, S., Brown, J., Colman, R., Delage, F., Power, S., Moise, A., & Zhang, H. (2020). Climate change projections for the Australian monsoon from CMIP6 models. *Geophysical Research Letters*, *47*(13), e2019GL086816. https://doi.org/10.1029/2019GL086816

Narsey, S., Reeder, M. J., Ackerley, D., & Jakob, C. (2017). A midlatitude influence on Australian monsoon bursts. *Journal of Climate*, *30*(14), 5377–5393. https://doi.org/10.1175/JCLI-D-16-0686.1

Narsey, S., Reeder, M. J., Jakob, C., & Ackerley, D. (2018). An evaluation of northern Australian wet season rainfall bursts in CMIP5 models. *Journal of Climate*, *31*(19), 7789–7802. https://doi.org/10.1175/jcli-d-17-0637.1

Neelin, J., & Held, I. (1987). Modeling tropical convergence based on the moist static energy budget. *Monthly Weather Review*, *115*(1), 3–12. https://doi.org/10.1175/1520-0493(1987)115<0003:MTCBOT>2.0.CO;2

Neelin, J. D., Martinez-Villalobos, C., Stechmann, S. N., Ahmed, F., Chen, G., Norris, J. M., et al. (2022). Precipitation extremes and water vapor: Relationships in current climate and implications for climate change. *Current Climate Change Reports*, *8*(1), 17–33. https://doi.org/10.1007/s40641-021-00177-z

Peters, M. E., Kuang, Z., & Walker, C. C. (2008). Analysis of atmospheric energy transport in ERA-40 and implications for simple models of the mean tropical circulation. *Journal of Climate*, *21*(20), 5229–5241. https://doi.org/10.1175/2008jcli2073.1

Pfahl, S., O'Gorman, P. A., & Fischer, E. M. (2017). Understanding the regional pattern of projected future changes in extreme precipitation. *Nature Climate Change*, *7*(6), 423–427. https://doi.org/10.1038/nclimate3287

Raymond, D. J., Sessions, S. L., Sobel, A. H., & Fuchs, Ž. (2009). The mechanics of gross moist stability. *Journal of Advances in Modeling Earth Systems*, *1*(3). https://doi.org/10.3894/JAMES.2009.1.9

Seager, R., & Henderson, N. (2013). Diagnostic computation of moisture budgets in the ERA-Interim reanalysis with reference to analysis of CMIP-archived atmospheric model data. *Journal of Climate*, *26*(20), 7876–7901. https://doi.org/10.1175/jcli-d-13-00018.1

Seager, R., Naik, N., & Vecchi, G. A. (2010). Thermodynamic and dynamic mechanisms for large-scale changes in the hydrological cycle in response to global warming. *Journal of Climate*, *23*(17), 4651–4668. https://doi.org/10.1175/2010jcli3655.1

Seager, R., Neelin, D., Simpson, I., Liu, H., Henderson, N., Shaw, T., et al. (2014). Dynamical and thermodynamical causes of large-scale changes in the hydrological cycle over North America in response to global warming. *Journal of Climate*, *27*(20), 7921–7948. https://doi.org/10.1175/jcli-d-14-00153.1

Seager, R., & Vecchi, G. A. (2010). Greenhouse warming and the 21st century hydroclimate of southwestern North America. *Proceedings of the National Academy of Sciences of the United States of America*, *107*(50), 21277–21282. https://doi.org/10.1073/pnas.0910856107

Sheng, B., Wang, H., Li, H., Wu, K., & Li, Q. (2023). Thermodynamic and dynamic effects of anomalous dragon boat water over south China in 2022. *Weather and Climate Extremes*, *40*, 100560. https://doi.org/10.1016/j.wace.2023.100560

Shepherd, T. G. (2016). A common framework for approaches to extreme event attribution. *Current Climate Change Reports*, *2*(1), 28–38. https://doi.org/10.1007/s40641-016-0033-y

Sobel, A. H., Nilsson, J., & Polvani, L. M. (2001). The weak temperature gradient approximation and balanced tropical moisture waves. *Journal of the Atmospheric Sciences*, *58*(23), 3650–3665. https://doi.org/10.1175/1520-0469(2001)058<3650:twtgaa>2.0.co;2

Suppiah, R. (1992). The Australian summer monsoon: A review. *Progress in Physical Geography*, *16*(3), 283–318. https://doi.org/10.1177/030913339201600302

Tonidandel, S., & LeBreton, J. M. (2011). Relative importance analysis: A useful supplement to regression analysis. *Journal of Business and Psychology*, *26*(1), 1–9. https://doi.org/10.1007/s10869-010-9204-3

Trenberth, K. E. (1999). Conceptual framework for changes of extremes of the hydrological cycle with climate change. *Climatic Change*, *42*(1), 327–339.

Trenberth, K. E., Fasullo, J. T., & Shepherd, T. G. (2015). Attribution of climate extreme events. *Nature Climate Change*, *5*(8), 725–730. https://doi.org/10.1038/nclimate2657

Wang, B., Jin, C., & Liu, J. (2020). Understanding future change of global monsoons projected by CMIP6 models. *Journal of Climate*, *33*(15), 6471–6489. https://doi.org/10.1175/jcli-d-19-0993.1

Weng, J., Wang, L., Luo, J., Chen, B., Peng, X., & Gan, Q. (2022). A contrast of the monsoon–tropical cyclone relationship between the western and eastern North Pacific. *Atmosphere*, *13*(9), 1465. https://doi.org/10.3390/atmos13091465